Design and Analysis of a Polar-Orbiting Gravimetry CubeSat-2

A Major Qualifying Project Report

Submitted to the faculty of
WORCESTER POLYTECHNIC INSTITUTE
In Partial Fulfillment of the Requirements for the
Degree of Bachelor of Science
in Aerospace Engineering
by

Liam Piper

Ethan Prigge

Approved by:
Michael M. Demetriou, Advisor
Professor, Aerospace Engineering Department

This report represents the work of one or more WPI undergraduate students submitted to the faculty as evidence of completion of a degree requirement. WPI routinely publishes these reports on the web without editorial or peer review. Certain materials are included under the fair use exemption of the U.S. Copyright Law and have been prepared according to the fair use guidelines and are restricted from further use.

Abstract

This report presents the design of a 12U Gravimetry CubeSat. Gravimetry Satellites carry sensors that measure gravitational readings over ice caps to map geophysical characteristics and help study climate change. CubeSats provide a cost-effective way to carry on the work of previous gravimetry missions. This 10-year mission uses two satellites at inclinations of 91 and 103 degrees to ensure global coverage. Orbital design was performed using Systems Tool Kit (STK®). A Gradiometer was developed with six high-precision accelerometers. Mechanical design was conducted in SolidWorks and Ansys. An Attitude Determination and Control System alongside an on-board computer and communications system was designed. Power generation, electric propulsion, thermal, and radiation effects were analyzed in STK®. The Polar-Orbiting Gravimetry CubeSat (POGSat) was designed to provide complete global mapping of the Earth's gravity field every three weeks, with a mission duration of 10 years, a marked improvement from previous gravimetry missions such as GOCE.

Acknowledgements

The authors would like to thank Professors Michael M. Demetriou and Zachary R. Taillefer for advising the CubeSat project from which this report resulted alongside the sister paper written by Jackson Neu and Ellie Sherman. The authors would also like to thank the student Nathaniel Polus for their assistance in this project.

Table of Contents

Table of Equations

Table of Figures

Table of Tables

Table of Authorship

Table 1: Table of Authorship

Section	Main Author(s)	Secondary Author	Editor(s)
Introduction	Liam Piper, Ellie Sherman, Jackson Neu & Ethan Prigge	N/A	Liam Piper & Ellie Sherman
GNC	Liam Piper	N/A	Ethan Prigge
ADCS	Liam Piper	Ethan Prigge	N/A
Power	Ethan Prigge	Liam Piper	N/A
ADC Testbed	Liam Piper & Ethan Prigge	N/A	N/A
Conclusion	Liam Piper & Ethan Prigge	N/A	N/A

1 Introduction

A CubeSat is a class of Satellite also known as Microsats. CubeSats conform to a size formfactor made up of units which are 10x10x11cm cubes. The main mission of this report is two Polar Orbiting Gravimetry Satellite(s) orbiting at different inclinations to ensure the best coverage of the Earth within a one-month period. This report divulges the general details relating to this mission and the design of the corresponding Attitude Determination and control system, Power system, Guidance, Navigation, Communication, Command and Data systems.

CubeSats originated as a project between California Polytechnic State University and Stanford University in 1999, these nano-satellites aim to streamline the processes of designing, constructing, and testing technologies within low Earth orbit. Constructed from units measuring 10 cm cubed—known as 'U's—CubeSats typically adopt 1U or 3U configurations, though recent advancements have led to the creation of larger models to accommodate more extensive mission payloads with sizes of 1U, 3U, 6U and 12U. Commonly launched via mechanisms attached to a rocket's upper stage, CubeSats provide a straightforward method for entering Earth's orbit. Initially conceptualized to enhance scientific and military space endeavors, CubeSats have evolved into critical tools for the scientific community, supported by initiatives like NASA's CubeSat Launch Initiative, which facilitates their deployment as secondary payloads on larger rockets.

1.1 Mission Objective

The primary objective of the Polar Orbiting Gravimetry Satellite (POGSat) mission is to conceptually design a pair of satellites to map the Earth's gravitational field with complete global coverage over a period of approximately one month. The two satellites will be deployed to low orbits of 260 km altitude, and inclinations of 91° and 103°. The two satellites at different inclinations will allow for greater global coverage within a one-month period. The continuously updated map of Earth's gravity measured by the satellites will allow the monitoring of mass movements on and within the earth, such as the melting of polar ice caps, or seismic activity.

1.2 Project Management

For this project, sub teams were divided among four students. Weekly meetings are held with the sub team leads and with faculty to facilitate systems engineering between the teams. The team also uses SMS and Microsoft Teams to communicate. Mission objectives outside of the sub teams are evenly distributed among the students. The air bearing table is split between Liam Piper and Ethan Prigge while the cage is split between Jackson Neu and Ellie Sherman. Any purchases required are facilitated through Jackson Neu.

1.3 Societal and Environmental Impacts

Climate change is a global challenge that affects the physical environment, ecosystems, and human societies. It is caused by the increase of greenhouse gases in the atmosphere, mainly due to the burning of fossil fuels. Some of the impacts of climate change include more frequent and intense heat waves, droughts, floods, wildfires, sea level rise, and loss of biodiversity. To understand and respond to climate change, we need reliable and comprehensive data on its causes and consequences. Spacecraft can play a vital role in providing such data, by observing

the Earth system from different perspectives and with various instruments. Spacecraft can help monitor the changes in the atmosphere, oceans, land, ice, and biosphere, as well as the interactions among them.

1.3.1 Ice Caps

One of the areas where spacecraft can contribute to climate change research is the study of the polar ice caps. The ice caps store a large amount of water and reflect solar radiation, thus influencing the global climate. However, they are also vulnerable to melting due to rising temperatures. Spacecraft can measure the mass, thickness, extent, and movement of the ice caps using gravimetry. The GRACE and GOCE missions have already demonstrated using gravimetry to detect changes in the Earth's gravity field ca used by the loss or gain of ice mass. Other methods before this used strictly indirect measurements to find the mass lost. It's also extremely important to continue updating this data with new missions to see whether the rate of ice lost is changing over time. This mission is targeting about the same monthly data points as GRACE but will be collecting new data and will have a higher resolution due to newer technologies [52].

1.3.2 Hydrology

Another area where spacecraft can help is hydrology, or the study of the water cycle and resources on Earth. Understanding the flow of water is vital to both human infrastructure and environmental systems. With the Earth's freshwater supply being less than 3% of its total water supply, the location and movement information of that water becomes a necessity. In the past, the GRACE mission found evidence of wetting of the upper and lower latitudes and drying of the middle latitudes. While the cause is unclear, it is important to continue to monitor the flow of water throughout the planet [52].

1.3.3 Oceanic Sciences

A third area where spacecraft can assist is oceanic sciences, or the study of the physical, chemical, biological, and geological processes in the oceans. The oceans cover about 70% of the Earth's surface and play a major role in regulating the climate by absorbing heat and carbon dioxide. However, they are also subject to changes such as rising water levels, which leads directly to energy imbalance of the Earth. Gravimetry can detect the mass changes in oceans and determine how the energy is balanced throughout the Earth, which is a direct indication of climate change. Another game changer for gravimetry is the ability to indirectly detect heating of the deep ocean. Currently, most ocean heating data is on the surface of the oceans and doesn't include lower depths, but combined with other satellite data, gravimetry can detect heating of the ocean below 2000m [52].

1.3.4 Disaster Management

A fourth area where spacecraft can support is disaster management, or the prevention, mitigation, preparedness, response, and recovery from natural or human-induced disasters. Disasters can cause significant losses of lives, properties, infrastructures, and ecosystems. Because of the monthly scale of the mission, our satellites will be able to predict drought and flood risk areas before they happen. Using the mass or lack thereof of water, our mission can accurately tell which areas have too much or too little water and compare it to how much water they had the month before [52].

1.4 Background

Many aspects of this project are based on prior gravitational measuring satellite missions, such as GOCE and GRACE which are discussed below. Our mission seeks to be the first gravimetry satellite in the CubeSat formfactor.

1.4.1 Gravimetry

Gravimetry is the measurement of a gravitational field. For this mission, a satellite will be used to measure Earth's gravitational field strength and its variation with position and time. The gravitational force due to Earths' gravity field has a relatively constant value of 9.81 $\frac{m}{s^2}$ however, there are slight variations in this force due to the mass distribution of Earth. The most significant effect is caused by the oblate shape of the Earth; however, smaller gravitational anomalies exist due to varying density and topography. The strength of these anomalies is on the order of 300mGal, where 1 mGal = $10^{-5}\frac{m}{s^2}$ [6].

Most models of the gravitational field use a spherical harmonic representation [7]. This model approximates the strength of the gravitational field with a sum of harmonics of varying strength and frequency, similar to a Fourier series. Computing the coefficients of each harmonic term provides an approximation of a gravity field that varies with latitude and longitude.

The study of Earth's gravity was an important area of science long before the first satellites were launched. Prior to the space age, gravimetric measurements were conducted with land-based equipment, however it was challenging to correlate measurements made by different instruments in various locations, and marine measurements were less accurate than those on land. Satellite based gravimetry allows for complete global coverage with a single instrument [9].

1.4.2 Polar Gaps

When performing missions that target the high-latitude polar regions, a percentage of the Earth remains uncovered by polar orbiting satellites due to the high inclination required to accumulate data in polar regions. In a single satellite configuration, this gap, as often dubbed "polar gaps" by researchers, is closed by an interpolation of the collected data, with the accuracy dependent on the amount of data collected and the size of the gap [48]. The gravity field from within these gaps can be recovered using a set spherical harmonic coefficient implemented into a spherical harmonic expansion, which allows for the calculation of a gravitational field given a set of position, velocity, and acceleration vectors [49].

$$V(\rho, \varphi, \lambda; \mathrm{u}) = \frac{GM}{\rho}\left[1 + \sum_{l=2}^{L_{MAX}} \sum_{m=0}^{l} \left(\frac{R_E}{\rho}\right)^l \left(\overline{C_{lm}} \cos(m\lambda) + \overline{S_{lm}} \sin(m\lambda)\right) * \overline{P_{lm}} \sin(\varphi)\right] \quad (1)$$

The recovered data calculated using the expansion formula is then compared to the collected gravitational field data to determine the accuracy of the full recovered gravity field.

A way to lessen the amount of interpolation is by widening the sample size, which is achieved by varying the inclination of orbits in a satellite constellation. A bender double-pair refers to a constellation of satellite pairs composed of one polar orbit with an additional pair, usually of a high inclination between 60° -70°, added to collect more data and improve data

resolution within the middle latitude region [49]. The addition of the second pair improves coverage along the polar region and decreases the time required to complete full global coverage.

1.4.3 GOCE Mission

The Gravity Field and Steady State Ocean Circulation Explorer (GOCE) was a satellite created by the European Space Agency (ESA) designed to monitor and map Earth's gravitational field. GOCE launched in March of 2009 into a low earth orbit of 260 km altitude. The mission came to an end in October 2013 [1].

The primary instrument of GOCE was the Electrostatic Gravity Gradiometer (EGG), which was used to create a map of earth's geoid. The EGG consisted of three pairs of highly sensitive accelerometers, mounted along three perpendicular axes, centered on the satellite's center of mass. The six accelerometers formed an instrument known as a gradiometer. The axes of the gradiometer were aligned to be earth facing, along track (parallel to velocity), and cross track (perpendicular to velocity). By positioning the accelerometers away from the center of mass, it was possible to measure the variation in gravitational force along the arms of the gradiometer. These measurements are used to construct the gravity gradient tensor at the satellite's location. The tensor, shown below, represents how the gravitational force vector is changing along each spatial dimension. Using this gravity tensor, the shorter wavelength terms of the gravity field can be derived.

$$G = \nabla g = \begin{bmatrix} \frac{\partial g_x}{\partial x} & \frac{\partial g_x}{\partial y} & \frac{\partial g_x}{\partial z} \\ \frac{\partial g_y}{\partial x} & \frac{\partial g_y}{\partial y} & \frac{\partial g_y}{\partial z} \\ \frac{\partial g_z}{\partial x} & \frac{\partial g_z}{\partial y} & \frac{\partial g_z}{\partial z} \end{bmatrix} \quad (2)$$

In addition to the gradiometer, GOCE employed Satellite to Satellite Tracking (SST) via GPS for additional gravity measurement. SST gravimetry works by precisely tracking the satellite's orbit using GPS, while measuring non-gravitational accelerations using onboard accelerometers. The GPS tracking of orbital perturbations can be used to derive differences in the gravitational force throughout the satellites orbit [4]. The SST technique accurately measures the longer wavelength terms of the gravitational field. By combining the EGG and SST, GOCE measured Earth's gravity field with an accuracy of $10^{-5}\,\frac{m}{s^2}$ at a length scale of 100 km [3].

1.4.4 GRACE and GRACE-FO

The Gravity Recovery and Climate Experiment (GRACE) mission was a joint mission between the National Aeronautics and Space Administration (NASA) and German Aerospace Center (DLR) with ground operations performed by the ESA and German Research Centre for Geosciences (GFZ). The GRACE satellite mission was conceptualized to monitor the Earth's gravitational field changes to map the Earth's water and mass redistribution over time [10]. The mission lasted from March 2002 to October 2017 [11]. After the GRACE mission concluded, a follow-up mission termed GRACE Follow-On (GRACE-FO) was launched in May 2018 with an identical mission description and similar payload with the goal of continuing GRACE's data collection efforts.

The primary instrumentation payload for GRACE included a three-axis capacitive accelerometer, which measures the non-gravitational forces acting on the pair of satellites as a function of their position [12]. Coupled with the accelerometer readings, a K-Band Ranging (KBR) System was installed to measure the distance between the leading and lagging satellites to measure the fluctuations in the gravitational field experienced by each satellite [11]. The true position of the satellites is confirmed using SST through the GPS constellation, which serves to establish the satellite's expected position at a given point within the satellites' orbit. The varying strength of the Earth's gravitational field will draw the leading satellite forward in its orbit, reflected by the by measurements from the onboard accelerometers and communicated between the satellites using the KBR System, allowing a map of the gravitational field to be constructed by mapping the orbital perturbations experienced by the GRACE satellite system.

The measurement accuracy obtained in the GRACE mission series was at a length of scale of 200 km at a $10^{-5}\,\frac{m}{s^2}$ scale [13].

1.4.5 MAGIC

Conceptualized to improve the data collection efforts of GRACE, the Mass Change and Geoscience International Constellation (MAGIC) Satellite constellation is a dual satellite-pair configuration developed by the ESA for launch in 2028 [14]. Structurally similar to the GRACE and GRACE-FO missions, MAGIC will map the Earth's gravitational field by measuring the orbital perturbations communicated between each satellite pair. To improve collection accuracy, MAGIC seeks to implement the improved gradiometer payload introduced in the GOCE mission, using three accelerometers to calculate a gravitational gradient instead of the axis-specific gravitational readings from the GRACE mission series. MAGIC is conceptualized to use a pseudo-bender constellation formation: composed of a pair of satellites that fly in an 89° polar orbit and a pair in a 70° high-inclined orbit. The validation for the addition of the second satellite pair is to improve coverage of the mid latitudes, decreasing the time required to achieve full global coverage [15]. Like previous gravitational mapping missions, MAGIC will have an altitude of 340 km and 355 km, for the polar and inclined satellite pairs, respectively, to maximize the gravitational field strength experienced by the satellites.

1.5 Mission Design

The mission design hinges on meticulously defined subsystem specifications, ensuring that each element contributes optimally towards the collective mission objectives.

1.5.1 Requirements

Payload: The payload, central to the mission, is required to have an exemplary measurement accuracy of 10^{-5} m/s^2 at a spatial resolution of 100 km, which necessitates state-of-the-art sensors and data processing algorithms. This is to ensure that there is sufficient resolution for good science being collected.

Power: The power subsystem is tasked with providing a stable and sufficient energy supply to all onboard systems throughout the mission. This will be achieved through an array of onboard solar cells, which must be capable of harnessing and storing solar energy efficiently.

ADCS (Attitude Determination and Control System): Precision is paramount for the ADCS, with a target pointing accuracy of 0.1 degrees, allowing for the fine-tuned orientation necessary for accurate data collection of the payload. The ADCS system also needs to have fast slew maneuver times.

GNC (Guidance, Navigation, and Control): The GNC subsystem will facilitate robust communication channels capable of at least 1 kb/s uplink and downlink speeds. Moreover, the onboard GPS system is expected to maintain a positional accuracy between 1-5 cm. The system also has to make sure that the CubeSat is pointing nadir-in at all times to keep the same reference frame for the payload data scheme.

1.5.2 Constraints

Payload: The deployment mechanism for the boom arms must ensure they are consistently oriented Earthward, and meticulously aligned both parallel and perpendicular to the velocity vector, with a critical alignment to the satellite's center of mass to avoid perturbing its stability.

Power: The power subsystem is constrained to guarantee an uninterrupted energy supply to all other systems, taking into account the mission's full duration, and considering the cyclical nature of solar energy availability in space.

ADCS: The ADCS system is constrained by the requirement to detumble and stabilize the satellite within two orbits post-activation. Furthermore, it must operate concurrently with the payload, ensuring data collection is uninterrupted and precise. The ADCS system will have no moving parts to reduce chance of machinal failure.

GNC: The design anticipates that the GNC's capabilities will exceed the basic requirements for data transmission and remote system updates. Additionally, the communications infrastructure will incorporate a dual redundancy protocol to safeguard against system failures.

1.5.3 Optimal Orbit

The optimal orbit for a gravitational field mapping mission should maintain a low altitude or extreme low earth orbit (eLEO) and have high inclination for global coverage. The payload needs to be constantly Earth-facing to provide accurate accelerometer readings. To maximize the experienced gravity on the satellite, the CubeSat will maintain a constant 260 km altitude. In addition to the primary 91° orbiting CubeSat, an additional CubeSat at a 103° inclination is needed to reduce the time required to establish global coverage from 42 days to 32 days. This modified Bender configuration will optimize the amount of gravitational field measured such that monthly field readings can be provided to researchers for a three-month sampling basis, which is typical for yearly ice-flow measurements [20].

1.5.4 Mission Phases

The satellite mission is split into phases indicative of different mission objectives. Due to the 22° inclination change required for a single deployment, to extend the duration of the Phase Two science phase of the mission the CubeSats will be deployed on two different Electron rideshare missions. As such, each deployment will be assumed to occur at or close to the two desired inclinations as specified.

Upon deployment from the Electron launch vehicle, the CubeSats will begin Phase Zero, categorized by each CubeSat performing a detumbling maneuver and system performance check. To perform a detumbling maneuver, the CubeSats will use onboard magnetorquers to counteract the angular velocity experienced after ejection from the launch vehicle. In addition to the detumbling maneuver, the onboard computer will perform a communication and systems check, ensuring that the ADCS system and payload accelerometers are within functional capacity. This

detumbling phase is critical to ensuring control of the CubeSat, as reducing the angular velocity will permit further attitude control to take place.

After Phase Zero is completed, the CubeSats complete a series of transfer orbits and plane changes to establish their intended inclination and altitude. Phase One is composed of an orbit lowering maneuver, wherein the CubeSats will maneuver into their target altitude and inclination, a polar orbit of 91° and high inclined orbit of 103°, both at a 260 km altitude. Provided an ideal deployment, the Electron launch vehicle will deploy each POGSat at their desired inclination at an altitude of 500 km, where each POGSat will perform an orbit lowering maneuver. If any additional inclination changes are necessary, it would occur within Phase One.

Once the POGSats are in their optimal orbit, Phase Two will begin. This phase is where the satellite will carry out its primary mission of taking gravity measurements. At the start of Phase Two, the satellite will deploy the gradiometer payload arms and begin collecting data. This phase involves station-keeping and drag compensation maneuvers necessary to prolong the data collecting portion of the mission. Station-keeping maneuvers will consist of orbit raising to maintain the target 280 km. Due to the extreme Low Earth Orbit (eLEO) altitude achieved by the CubeSats within this mission, drag compensation will need to be performed to maintain the ideal orbit for data collection. This period should be around 10 years in length to ensure long term scientific coverage.

After Phase Two concludes, the CubeSats will need to deorbit within 5 years in accordance with FCC regulations [17]. Within Phase Three, CubeSats will perform a final orbit lowering maneuver to reduce altitude to 75 km, which is the accepted altitude that most satellites deteriorate upon reentry [18]. Table 1 summarizes the mission phases and maneuvers.

Table 2: Mission Phase Diagram

Mission Phase	Maneuvers	Description
Phase Zero	Launch Vehicle Separation	Detumble satellites
	System Performance Check	Initialize onboard systems to confirm functionality
Phase One	Orbit Lowering	Reduce altitude from deployment to target altitude
	Plane Change	Adjust inclination from deployment inclination, if necessary
Phase Two	Gravimetry Mission	Perform gravitational field measurements
	Orbital Maintenance	Station-keeping burns to raise altitude
	Drag compensation	Eliminate non-gravitational forces experienced by the satellites
Phase Three	Deorbit	Lower orbit to incite burnout

1.5.5 Launch Vehicle

As part of our mission plan, we needed to choose a vehicle to bring POGSat into orbit. Nearly all common launch vehicles have the capability to deploy a lightweight CubeSat into low earth orbit, and most launch providers offer rideshare services for SmallSat missions, helping reduce the cost of launch. For our mission, we considered proven vehicles such as the Falcon 9, Electron, and Atlas 5, all of which have flown with our selected satellite dispenser. The Atlas 5

rocket is soon to be retired, so we chose between the Falcon and Electron. Both vehicles are more than capable of supporting our mission as part of a rideshare launch and have excellent flight heritage. Ultimately, we opted for the Electron for a few reasons. The Electron is specifically designed for SmallSat launches and rideshare missions, having completed 11 such missions. The Canisterized Satellite Dispenser we are using is created by Planetary Systems Corporation, a subsidiary of Rocket Lab, meaning the dispenser is easily integrated onto the Electron rocket. Finally, the Electron has a unique third stage called the "Kick Stage", which is designed to perform orbital adjustments for rideshare missions, to deploy satellites to multiple desired orbits in one mission [3]. This capability should allow us to deploy the satellites close to our target orbit.

1.5.6 Payload

The scientific payload for the mission is a three-axis gradiometer, similar to the instrument used on GOCE. The gradiometer is comprised of three paired accelerometers, which allow a differential measurement of the gravity field by the process outlined in Section **Error! Reference source not found.**. The accelerometer pairs are separated along the velocity vector (Z), earth facing vector (-Y), and cross-track vector (X), and intersect the center of mass. The accelerometers are separated by distances of 14.0, 17.7, and 16.8 cm across the X, Y, and Z axes respectively, forming the arms of the gradiometer. **Error! Reference source not found.** shows the gradiometer payload with the positive X, Y, and Z axes indicated. The six accelerometers are shown in black.

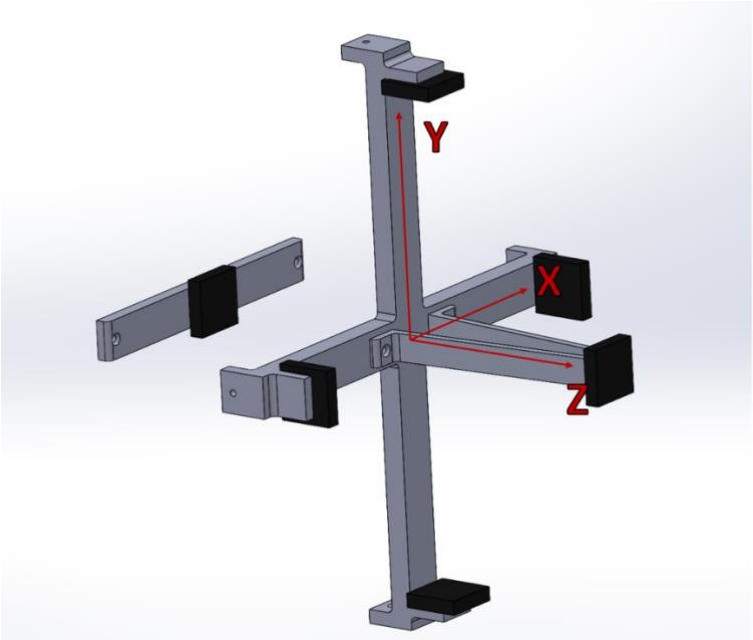

Figure 1: Gradiometer Payload Soildworks model.

In order for the gradiometer to collect accurate data, the axes of the gradiometer must be aligned with the spacecraft's center of mass during the entire science phase. This requires the location of the center of mass to not change as propellant tanks are drained. The locations of propellant tanks were adjusted such that their mass is balanced about the center of the gradiometer. Figure 1 shows the position of the center of mass aligned with the gradiometer for

both the fully fueled spacecraft and dry mass. The center of mass moves by only 1 mm between configurations.

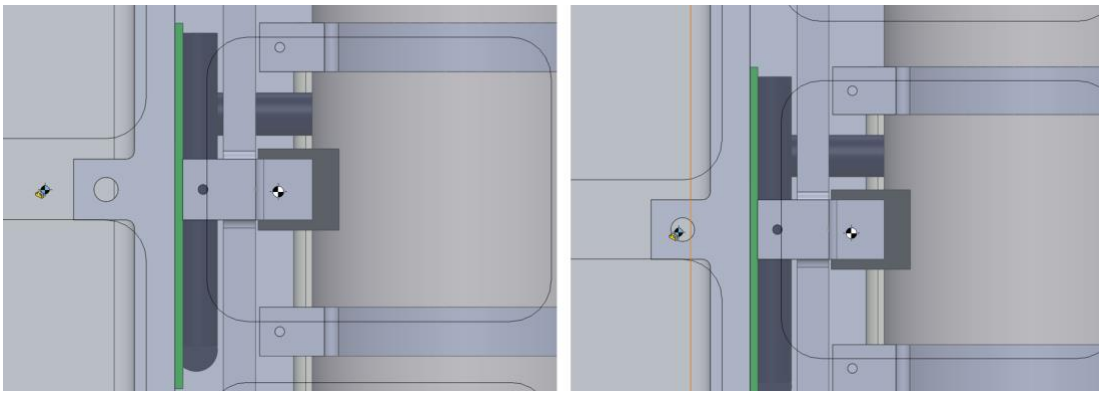

Figure 2: Center of Mass aligned with the gradiometer.

1.5.7 Accelerometer Instrument

The type of accelerometer used is a vibrating beam accelerometer (VBA). It is a newer type of accelerometer that uses a quartz wafer. As seen below in Figure 3, a close-up of the wafer can be seen where the seismic mass will vibrate within the decoupling frame and induce a change in resonance to determine the change in acceleration of the sensor.

VBAs are predicated on Hooke's Law, which states that the force needed to extend or compress a spring by some distance scales linearly with respect to that distance. In the context of a VBA, a quartz beam acts akin to a spring. The beam has a natural resonant frequency, given by

$$f = \frac{1}{2\pi}\sqrt{\frac{k}{m}} \tag{3}$$

where k is the effective spring constant of the beam and m is the seismic mass. When an external acceleration is applied, the seismic mass exerts an additional force on the beam, altering the effective spring constant, and thus the resonant frequency shifts proportionally.
This frequency shift Δf due to acceleration a can be described by

$$\Delta f = f_0\left(1 + \frac{a}{g}\right) \tag{4}$$

Where f_0 is the resonant frequency at rest, and g is the acceleration due to gravity. The sensitivity of the VBA, defined as the ratio of the frequency shift to acceleration, can be crucial for calibration purposes.

To achieve the high precision necessary for gravimetry, the VBA is encapsulated in a vacuum to minimize damping forces on the beam, such as air resistance, that would otherwise decrease the quality factor Q of the resonator. The quality factor is defined as

$$Q = \frac{f_0}{\Delta f_{half-power}} \tag{5}$$

Where $\Delta f_{half-power}$ is the bandwidth of the resonator at half power. A high Q indicates a sharper resonance peak, allowing for more accurate determination of frequency shifts.

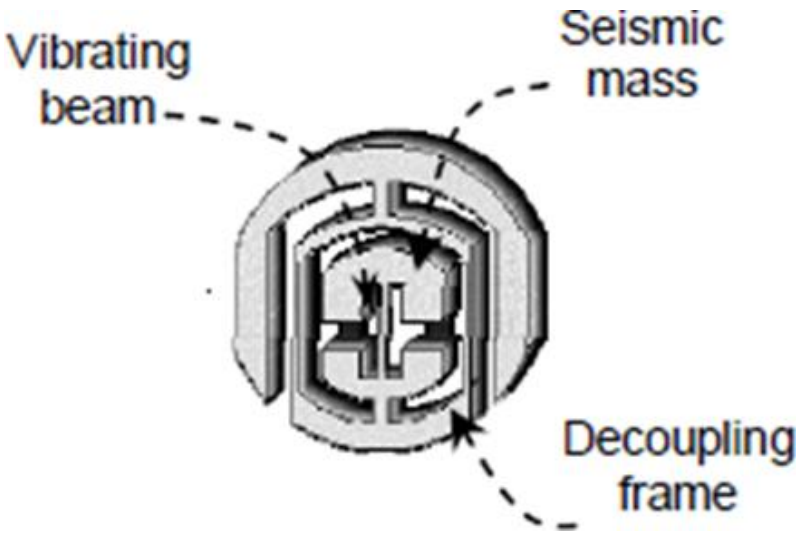

Figure 3 : Basis of the wafer. (Courtesy of IEEE) [1].

The accelerometer's output stability over time, a key metric of its performance, is assessed by measuring the Allan Deviation, which is used to characterize time-dependent errors in precision oscillators. The Allan Deviation provides insight into the types of noise affecting the VBA and its long-term stability.

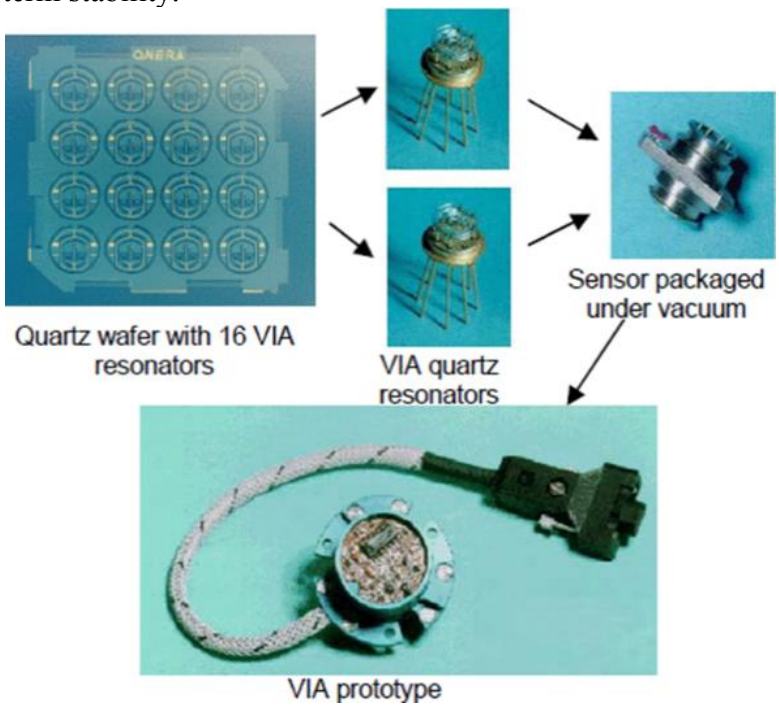

Figure 4 : Process of Wafer to VIA prototype (Courtesy of IEEE) [1].

In the characterization process on a tilt platform, the device's sensitivity to orientation with respect to gravity is determined, which follows the equation.

$$S = S_0 \cos(\theta) \quad (6)$$

With S_0 being the scale factor at zero tilt and theta being the tilt angle. This is vital as it affects the accuracy of the VBA when used in different orientations during the satellite's orbit.

Lastly, temperature effects are accounted for through thermal compensation techniques. As the material properties of the quartz, including the spring constant k and the seismic mass m, are functions of temperature (T), the resonant frequency is also a function of temperature, described by

$$f(T) = f_0[1 + \alpha(T - T_0)] \tag{7}$$

Where α is the temperature coefficient of the resonant frequency, and T_0 is a reference temperature for the sensor.

1.5.8 Data Collection

The data acquisition process on the spacecraft is a critical pathway to success for the mission. In this intricate procedure, an array of data is captured and stored, comprising raw sensor inputs and processed information. The raw data emanates directly from the onboard sensors, capturing a spectrum of gravitational metrics. Concurrently, the Attitude Determination and Control System (ADCS) works diligently to refine this raw data. Through the utilization of an Extended Kalman Filter, the ADCS outputs a "cleaned" version of the data. This advanced filtering technique is pivotal for isolating the true gravitational signals by correcting for potential noise and biases introduced by the movement of the satellite and other environmental factors. The ADCS also embeds critical attitude data corresponding to the exact time of each reading, which is essential for precise data alignment and subsequent analysis. Both sets of data, raw and processed, are then meticulously logged in a structured format, enabling efficient retrieval and transmission from the spacecraft back to Earth for further analysis.

1.5.9 Data Analysis

The data analysis process for the Polar-Orbiting Gravimetry CubeSat (POGSat) mission is a meticulous and sequential procedure that enhances the utility of raw sensor data, transforming it into a scientifically valuable asset. The process begins with data preprocessing, a foundational stage that ensures the integrity of the dataset through the removal of anomalies and the rectification of incomplete records. Data points that are missing are judiciously handled through methods such as interpolation, while the entire dataset is standardized into a uniform format for ease of analysis.

Following the initial cleansing phase, data exploration commences. This stage is characterized by the computation of descriptive statistics and the crafting of visualizations to form a preliminary understanding of the data's underlying structure. These exploratory steps are crucial for affirming the data's alignment with expected sensor performance. Next, the critical task of data calibration is undertaken, where accelerometer readings are meticulously adjusted using known calibration parameters to account for any instrument bias and scale errors. This ensures the subsequent gravity calculations reflect precise measurements.

The calibrated data then undergoes a coordinate transformation to align with the Earth-centered Earth-fixed (ECEF) system, crucial for the geolocation of gravitational data. This sets

the stage for the gravity calculation step, where algorithms and models are applied to the transformed data to extract gravity anomalies, providing insights into the Earth's gravitational field. The gravity calculations are then visually represented through geographic mapping using Geographic Information Systems (GIS), creating detailed maps that depict variations in gravitational strength.

The integrity of these calculations is affirmed in the data validation step, where the satellite-derived measurements are cross-referenced with established gravitational models to verify their accuracy. This is followed by rigorous statistical analysis, where statistical tests assess the significance of gravity variations, and uncertainty quantification measures are applied to ensure the data's reliability.

Interpreting these results is pivotal and involves correlating gravity anomalies with geological features and other Earth systems, thereby offering a deeper understanding of planetary dynamics. Finally, the comprehensive reporting stage documents the entire analytical process, encapsulating methodologies, results, and conclusions, and communicating the mission's findings to the broader scientific community and relevant stakeholders.

In summary, each step of this intricate data analysis process, from initial preprocessing to final reporting, is designed to ensure that the data collected by POGSat is not only accurate but also serves as a meaningful tool for advancing our understanding of Earth's gravitational field and its environmental implications.

2 Guidance, Navigation and Communication (GNC)

The Guidance, Navigation and Communication system is a separate but also integrated system with the ADCS. It is key to telemetry of the spacecraft, the prediction of the trajectory and communications for data and control [54]. The GNC System can also be known as telemetry in other space systems. GNC is the heart and core of every spacecraft and thus it needs to be figured out before the rest of the electronics or avionics of the spacecraft.

2.1 Onboard Computer & Flight Computer System (OBC & FCS)

For the CubeSat there needs to be a main computing module. This is handled by the OBC & FCS. Please note that these may be interchanged but they have the same meaning. The job of the OBC is to handle all telemetry, data and computational work for systems such as the ADCS.

Figure 5: ISIS iOBC SBC (Courtesy ISIS) [60].

The COTs unit selected was the ISIS on-board-computer (iOBC). It is rather low profile in a PC/104 formfactor so it works very well in the setting of a CubeSat. Additionally, factors such as low operating power, minimal weight and a decent computational core of a 32-bit ARM9 processor at 400Mhz. The iOBC also has multiple modes of interfaces for sensors, data streams and the like. These modes include UART, GPIO and I2C [60]. Lastly, the iOBC has significant flight history and experience.

To ensure that the OBC can handle the work of the ADC system, the code in MATLAB was converted to rough C code and was simulated using tispice to ensure that the computational work needed of the OBC could be met in real time and it was effective to be able to work ~3.75x faster than real time. This figure is important as this means that for a non-COTs unit, the computer could be less powerful and perhaps even smaller than the COTs unit needed to get the job done.

2.2 Guidance

The guidance part of GNC is broken up into three main sections: target denomination, trajectory planning and maneuver planning.

2.2.1 Target Determination

Guidance systems determine the desired position and velocity of the spacecraft, considering the mission objectives and orbital parameters. This information is often provided by mission planners and updated in real-time as needed. For this project it is to keep the spacecraft orienting in the same direction throughout the orbit pointing nadir-in. This topic is touched on further in the Attitude Determination and Control System (ADCS).

2.2.2 Trajectory Planning

Guidance systems calculate the optimal path or trajectory that the spacecraft should follow to reach its target or achieve specific mission goals. This includes determining when and how to perform maneuvers such as orbit changes and orienting the spacecraft using slew maneuvers to keep a certain orientation for science or maneuvers.

2.2.4 Maneuver Planning

Guidance systems plan and schedule propulsion maneuvers, which involve firing the spacecraft's thrusters to change its velocity or trajectory. These maneuvers are essential for maintaining the desired course and avoiding obstacles or hazards. This system relies on the propulsion system which is outlined in the sister MQP.

2.3 Navigation

Position Estimation: Navigation systems use various sensors and instruments, such as star trackers, gyroscopes, accelerometers, and GPS (when applicable), to continuously estimate the spacecraft's position and velocity in space. These measurements are critical for determining the spacecraft's current state relative to its intended path.

2.3.1 GPS System

A key and critical factor in the GNC and ADCS of the spacecraft is the GPS system to determine where the satellite is located in space. The system also needs to be highly accurate, up to 1-5cm of accuracy. This cannot be done with any GPS chipset, as the vast majority of consumer versions are accurate to 16ft. Additionally, these consumer versions are deactivated once it detects the GPS is moving 200mph or its altitude is above 60,000ft. Another thing to consider is the use of several positioning networks for higher accuracy. This can be done in a system that uses global navigation satellite systems (GNSS) [54].

Figure 6 : Example ublox GPS chipset (one of three useable) Courtesy of ublox [56]

A large problem of GPS COTS are that they are either not accurate enough or if they are then they are not rated for space applications and for the very small subset that does not fall into either category are systems designed for space with high precision and all of the commercial version are simply too large and normally much more expensive than needed. As a result, it would be better to design and make one purpose built for this mission.

For this mission the GPS ideally would be accurate to within ±1cm for location, this can be achieved using some of the highest quality GPS chipsets made by ublox. Additionally, it needs to implement GNSS support and RTK support alongside performance-made antennas. RTK stands for real time kinetics and using computational math it can fix many accuracy issues with GPS and dramatically impact our results for the better. These chips are significant as they display very high reliability and accuracy alongside have flight history.

The current performance of the prototype is accuracy is ±2 cm, working towards 1.5cm. With a typical cold fix time of 90 seconds and an estimated hot fix time of 30 seconds. These performance characteristics are within the ranges required by the ADCS system.

2.3.2 Sensors & Telemetry

For the ADC system it uses a variety of sensors to determine the current attitude. These include but are not limited to the gyroscope, accelerometers magnetometer and sun sensors.

Table 3: Sensor Data table

Sensor Name	**Manufacturer**	**Serial Number**	**Accuracy**	**Mass**
Gyroscope	Analog Devices	ADXRS453	131 LSBs/dps Up to +/- 300dps	2g
Payload Accelerometers	N/A	N/A	$2*10^{-12}$ m/s^2	15g
Accelerometers	ST	IIS3DHHC	±2.5 full scale	2g
Magnetometers	Honeywell	HMC2003	40 ugauss resolution 1 V/gauss sensitivity	2g
Sun Sensors	SOLAR MEMS	ISSDX-D60	FOV: 120 degrees Precision: 0.06 degrees	15g
GPS	Ublox	ZED-F9P-00B-02 NEO-M8P-2 NEO-6M-0-001	N/A	5g

2.4 Communication

Communication is a critical part of any satellite. It allows for the remote access of data. It also allows for the changing of the flight software if there are any bugs or problems if necessary.

2.4.1 Iridium

As the main communication system, it needs to be able to work wherever the satellite is in orbit. There are existing satellite communication networks such as Global Star and Iridium. We are using Iridium as it has been flight proven.

Figure 7 : Iridium 9602 module (Courtesy Iridium) [58].

This unit is the Iridium 9602 module and is rather small and light for a main communications system. Considering its size, it is very capable. It can communicate at a moderate 1.4 kilobytes/second (kb/s). The Iridium network has pole-to-pole coverage meaning that there is no data loss. This unit also happens to have significant flight heritage, having flown on many similar missions and being implemented in numerous capacities throughout different industries [58].

2.4.2 UHF

While the majority of communications will be done with Iridium there could be a problem with the system. So, a backup system is needed. With a UHF radio the CubeSat will be able to have additional points of contact for a data stream. The satellite would communicate with a ground station located at WPI in Worcester. However, with the flexibility of a UHF radio system its downlink could be received by many radio sites across the world expanding the ability to have communication points other than in Worcester, MA. Moreover, using a method of data transmission that is popular such as LoRAWAN would increase the possibility of a greater number of available ground stations.

Some basic goals of the UHF radio system are to be a backup communications system to the Iridium unit and to be able to handle higher data rates to the main system to allow for higher redundancy in the transmission of the data packets themselves. An ideal radio would have a RF transmission power of at least 1 watt and ideally at least 2-watts of power to help ensure a strong enough signal for a ground station to receive it clearly as with the majority of data transmissions the signals are digital and so either the packet makes it, or it doesn't.

Another thing to consider is the method/mode of data transmission, similar to the internet radios using packets of data to transmit over the air. There are a multitude of different modulation types. For our purposes GMSK is the ideal modulation type.

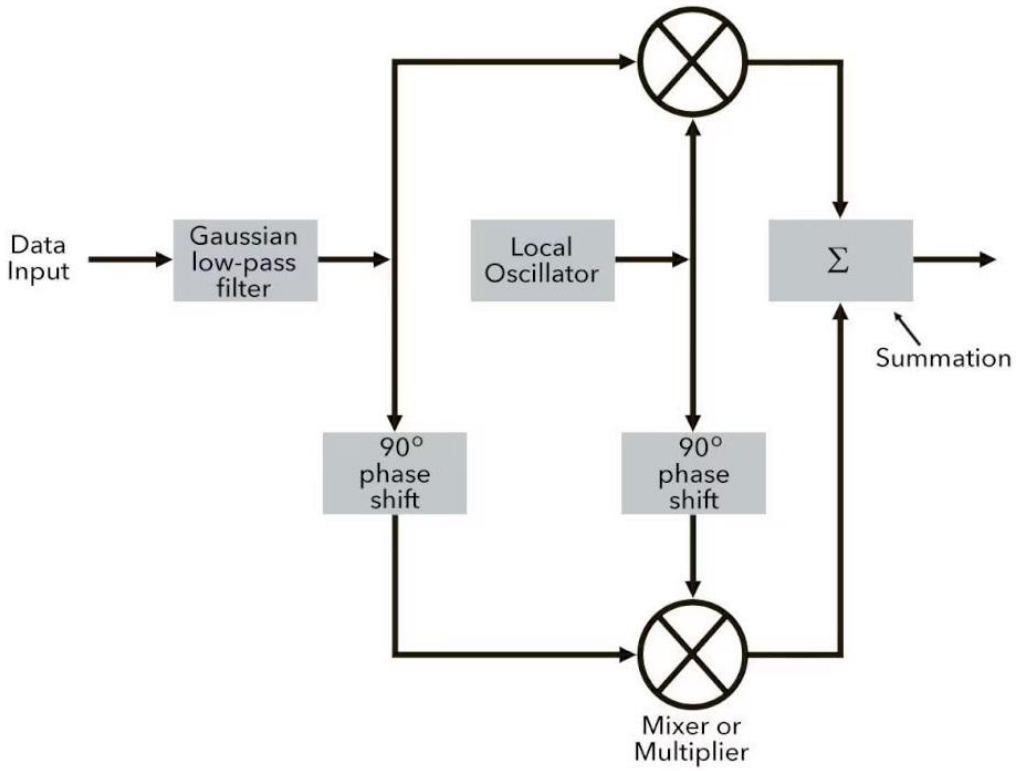

Figure 8 : Basic GMSK block-diagram (Courtesy of Analog Devices) [57].

The basic flow of the GMSK system can be seen above in Figure 8. Integrating GMSK into the POGSat CubeSat communication system incorporates technical aspects that suit the rigorous demands of space communication. GMSK's application of the Gaussian filter effectively smoothens phase transitions in the signal, reducing spectral bandwidth. This is critical to avoid interference in the limited available spectrum. Its constant envelope signal, resulting from the continuous phase property of GMSK, permits the use of power-efficient class C or E amplifiers, which is advantageous due to the limited power resources on CubeSats.

Furthermore, the resilience of GMSK to variations in signal amplitude makes it less susceptible to the effects of multipath fading, which is common in satellite communication. The modulation process involves a pre-modulation Gaussian filter to shape the frequency transitions, followed by a minimum shift keying (MSK) modulator that maintains a constant envelope. The demodulation can be achieved through a coherent detector that employs a phase-locked loop (PLL), simplifying the receiver design. The technical suitability of GMSK for the POGSat lies in its spectral efficiency and the robustness of the modulation in the face of the space environment's noise characteristics. This allows for reliable data transmission, ensuring the fidelity of crucial scientific measurements relayed back to Earth.

2.3.3 COTS UHF System

A commercial off the shelf Ultra High Frequency (UHF) backup/redundant system that would be great is the Endurosat UHF system. This system has an excellent track record and has many different operational modes. While it is very well made and is well suited for this application the system itself is rather expensive as a secondary communication system.

Figure 9 : Endurosat UHF TRANSCIEVER II (Courtesy of EnduroSat) [59].

Endurosat UHF TRANSCEIVER II. It has a maximum data transmission rate of 19.2 kb/s. The RF power of one watt. Modulation modes: GMSK, 2FSK and 4GFSK. As previously mentioned, this has significant flight heritage. The radio is designed to work with Endurosat's own lineup of flight computers, however, well will not be using their platform as the cost involved is not ideal and the specifications of their flight computers are not exactly what we are looking for [59]. There is an alternative UHF Unit in Appendix E.

2.4.5 Antennas

For the CubeSat there will be several Antennas for the communications system and the GPS systems. There are several factors when considering spacecraft designs such as the frequency on TX and RX, the grounding of the antenna, polarization, directionality, and many more such as impedance matching.

2.4.5.1a GPS Antennas

New Antenna for non-COTs GPS Sub-system, for the design of the antenna array it needs a center frequency, for a GNSS GPS system is 1575.42 MHz for the non-COTS system we will have a main antenna and a secondary array of Antennas (2x). The array is made up of one Microstrip Infed Patch Antenna and one Planar Inverted-F (PIF) Patch Antenna.

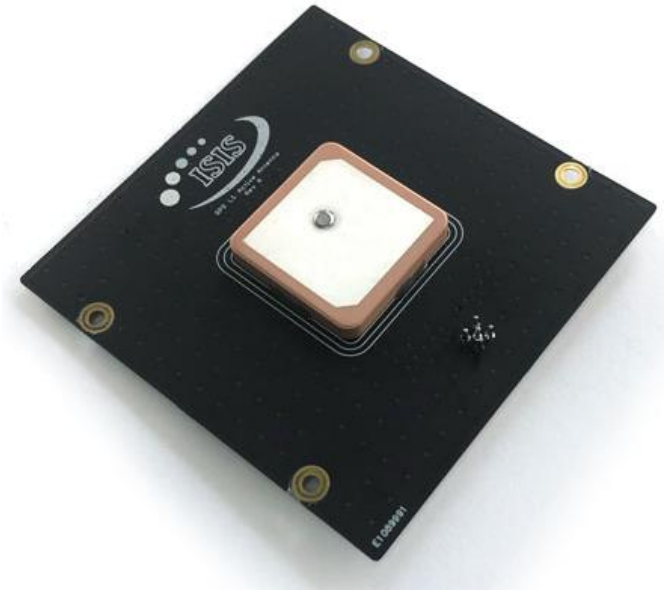

Figure 10: ISIS GNSS Active Patch Antenna (Courtesy of ISIS) [64].

The ISIS GNSS Active Patch Antenna represents a crucial component in the engineering of CubeSat systems, particularly in enhancing the capabilities and reliability of their GPS sub-systems. Designed to be compact and lightweight, with a mass of approximately 14 grams, this antenna is perfectly suited for the stringent size and weight constraints of 1U CubeSat platforms, which are small satellites with dimensions of 70x70x9.7mm [64]. The antenna boasts a gain of up to 5.5 dBi, ensuring effective communication and navigation capabilities by improving signal reception quality from GNSS (Global Navigation Satellite System) satellites [64]. The decision to equip a CubeSat with two of these antennas for redundancy is a testament to the meticulous planning that goes into satellite design, aiming to safeguard against the failure of a single antenna which could compromise the mission. This redundancy is vital for maintaining the integrity and operational continuity of the satellite's GPS sub-system, crucial for tasks such as orbital positioning, navigation, and timing. The ISIS GNSS Active Patch Antenna is thus a pivotal element in the modern CubeSat architecture, embodying the advancements in miniaturization and reliability that define contemporary satellite technology. Due to these reasons, they were picked as the main GPS antenna systems due to their flight experience and due to their high accuracy and reliability.

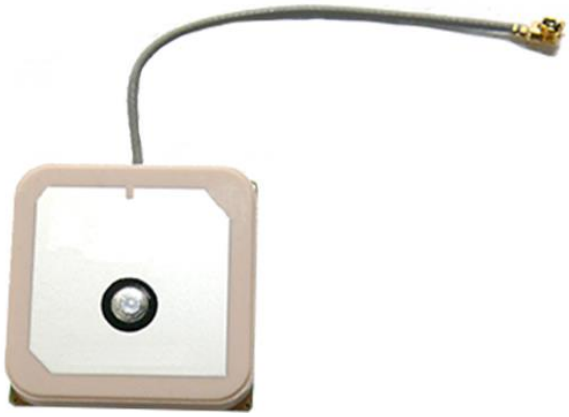

Figure 11: EXA GCA01 – Compact GNSS Active Patch Antenna (Courtesy of Ecuadoran Space Agency) [65].

Following the primary ISIS GNSS Active Patch Antenna, the CubeSat's design incorporates the EXA GCA01 – Compact GNSS Active Patch Antenna as its backup GPS antenna array. This choice underlines the critical nature of maintaining constant and accurate GPS functionalities within the satellite's subsystem [65]. The EXA GCA01 antenna is even more compact and lighter than its primary counterpart, with dimensions of 25x25x5mm and a weight of just 11 grams, making it an ideal solution for space-constrained applications [65]. Despite its diminutive size, the antenna offers a respectable gain of up to 4.75 dBi, ensuring it can reliably fulfill its role in the GPS subsystem by providing satisfactory signal reception from GNSS satellites in the event the main antenna system fails or underperforms [65].

This strategic inclusion of the EXA GCA01 as a backup antenna highlights the attention to detail and the emphasis on redundancy within CubeSat missions with high-stakes science missions such as the POGSat. By opting for this antenna, satellite designers demonstrate their commitment to operational reliability and the success of the mission, recognizing that even the smallest components, such as GPS antennas, play a significant role in the overall performance and safety of space operations. The selection of the EXA GCA01, with its compact profile and efficient performance, exemplifies the innovative solutions that are being employed to overcome the challenges of space technology, ensuring that CubeSats can achieve their objectives even under constrained conditions.

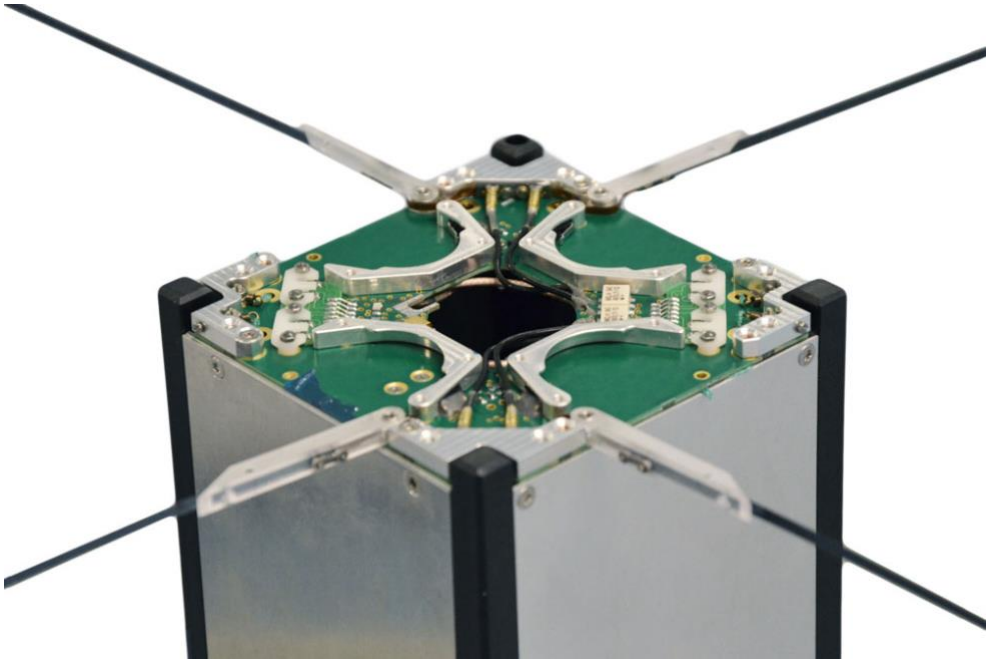

Figure 12: ISIS CubeSat UHF/VHF Antenna System (Courtesy of ISIS [66]).

The backup communications system for the CubeSat incorporates the ISIS CubeSat UHF/VHF Antenna System, a strategic choice that underscores the importance of ensuring robust and reliable communication channels in satellite operations. This antenna system, with a gain of up to 5.5 dBi, is designed to operate on the UHF (Ultra High Frequency) and VHF (Very High Frequency) bands, offering a versatile solution for both uplink and downlink communications [66]. Weighing 80 grams and measuring 98x98x7 mm, it presents a good balance between performance and the physical constraints of CubeSat platforms, especially considering the need for minimal weight and space utilization onboard [66].

This UHF/VHF antenna system serves as a critical backup to the primary communication system, prepared to take over should any unforeseen issues compromise the main channel. The selection of this antenna, with its considerable gain and designed dimensions, reflects a comprehensive approach to mission planning, where redundancy is not merely an option but a necessity for the success and longevity of the mission. The ISIS CubeSat UHF/VHF Antenna System embodies the commitment to resilience and reliability in CubeSat communications, ensuring that, regardless of circumstances, the satellite maintains its ability to communicate effectively with ground stations, thereby safeguarding the mission's objectives and data integrity.

3 Attitude Determination and Control System (ADCS)

The Attitude Determination and Control System is a mission critical system of the satellite. It handles operations such as orientation of the spacecraft, detumbling and controlling the spacecraft for thrust maneuvering and science. The payload requires one of the sensors booms to be always facing the Earth, which will be one of the main functions of attitude control. This MQP uses a combination of two methods for attitude determination and two control systems for attitude control. For the CubeSat to determine its attitude it needs four separate vectors, two in inertial frame and two in body frame. The sensors chosen to determine this are sun sensors and magnetometers alongside accelerometers, gyroscope, and a GPS system to help supplement the main sensors by giving helpful and relevant data.

Table 4: ADCS Mode Table

Mode	**What Happens in the Mode**
Mode 0	Detumble Mode
Mode 1	Maneuver Burn & Propulsion
Mode 2	Science Mode

Mode 0 is the detumble mode which will be expanded on later in this chapter. Mode 1 is the burn and propulsion mode for orienting the spacecraft to do burns only and not for the science sections of the flight. Mode 2 is the science mode in which the z-axis is pointing nadir-in, and the x-axis will be always facing the velocity vector.

3.1 ADCS Hardware

Actuators are what applies control torques to the spacecraft. Some examples actuators include reaction wheels, magnetorquers and thrust actuators. For this CubeSat, we will be using a magnetorquer. The other options are much more complex and would add significant mechanical complexity to the satellite. The ideal output torque of around 0.1 or less Nm. Ideal power usage of an axis of 3 watts or less. Diameter of coil: 1cm. Number of turns in the coil ~350 [55].

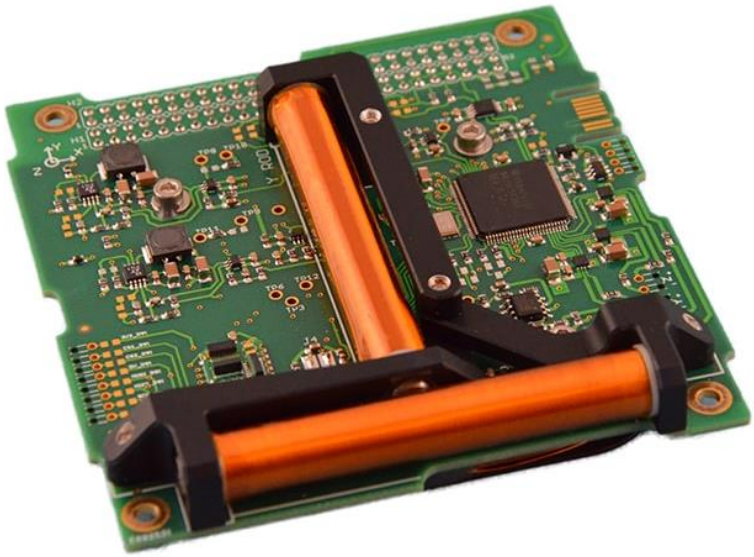

Figure 13 : iMTQ Magnetorquer board Courtesy of iMTQ [60]).

For a commercial off the shelf, one of the best options for a magnetorquer is one made by ISISPACE and their iMTQ Magnetorquer Board. Available volume is very limited in the CubeSat and this magnetorquer can only apply 0.001Nm without taking up too much space [60]. For operating the magnetorquer, a board might have to be designed to integrate it into the CubeSat. However, this system is rather limited in flexibility and strength of actuators and thus we need a more modular system. Moreover, it is only a high control board in 2-axis and not 3-axis which is necessary for the success of the POGSat mission in which we need maximum control of the orientation of the spacecraft. The iMTQ board is a better fit for smaller and less ADCS heavy missions.

Figure 14 : Gen 2: CubeTorquer (CR0006) Courtesy of CubeSpace [61].

For an independent system torque rod, the Gen 2: Cube Torquer (CR0006) by CubeSpace is a great option as it is very power efficient, low profile and powerful enough to do our necessary detumbling and slew maneuvers throughout the mission duration. It has an actuation strength of 0.6 Am^2 [61]. This was within our designed tolerance and fits what is expected of the system given our needed maneuver times and moment of inertia.

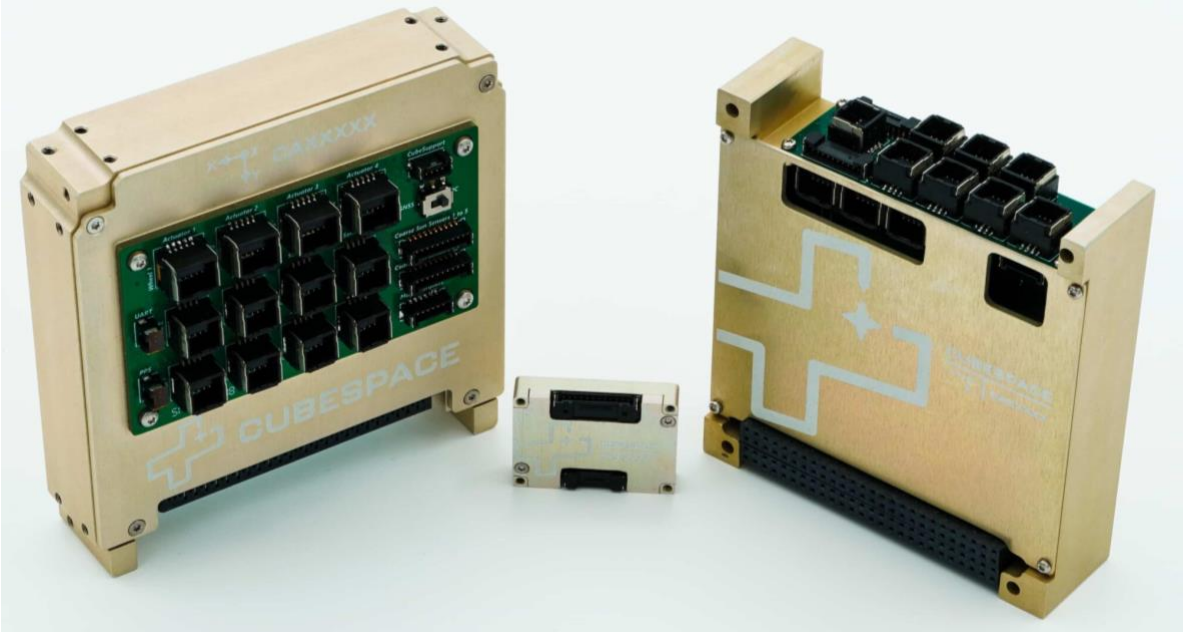

Figure 15 : CubeADCS Core (Courtesy of CubeSpace) [62].

Above is a magnetorquer controller, known as the Gen2: CubeADCS Core which is designed to interface with our selected COTs Magnetorquer. The job of the core is to be the interface or rather, be the in between of the torque rods and the controller itself, this takes the control laws and applies them using a digital to analog (DAC) converter which will apply the needed power which will induce the needed magnetic field.

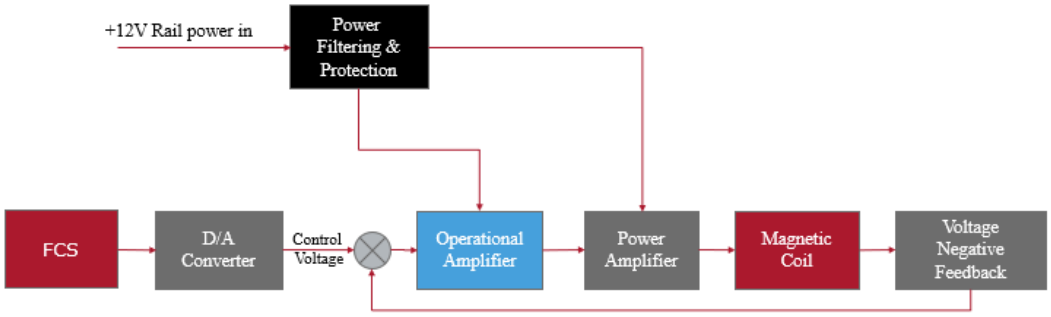

Figure 16: Magnetorquer Control Electronics Flow Diagram.

Above in Figure 16, the magnetorquer control electronics can be seen. This is an exploded version of the CubeADCS core in what it does and the sub-functions of the system within. The most important sections are the fight computer system (FCS) which includes the ADCS system which will be controlling the system from the outside. The D/A converter is a digital to analog converter which converts the digital control law of ones and zeros into an analog system as a control voltage. It is a control voltage as the magnetorquer runs off a constant current and therefore you can control the power of the magnetic field using just voltage. This control voltage is plugged into an operational amplifier which amplifies the voltage from the smaller range of the D/A to a larger range which in turn can directly affect the magnetic coil (magnetorquer) in which the system is connect to the voltage negative feedback loop to ensure the magnetic coil is not constantly on.

3.1 Static Determination

Knowing the spacecraft's position and direction relative to a fixed reference frame is essential for any space mission. This data is used by the control system to adjust the spacecraft's attitude and keep it on the correct orbit. There are two main ways to estimate the spacecraft's attitude: static and dynamic. For this MQP, both will be used, but static estimation will only be used as a supplement to dynamic estimation.

3.1.1 TRIaxial Attitude Determination (TRIAD)

This is one of the simplest forms of static attitude determination and relies on 4 vectors to work. Two of these vectors are body fixed and two are reference vectors. Using these 4 vectors, the TRIAD algorithm computes the attitude matrix by way of rotational matrices.

$$\hat{A}_{TRIAD} = \boldsymbol{b}_1 \boldsymbol{r}_1^T + (\boldsymbol{b}_1 \times \boldsymbol{b}_x)(\boldsymbol{r}_1 \times \boldsymbol{r}_x)^T + \boldsymbol{b}_x \boldsymbol{r}_x^T \tag{8}$$

Where $\hat{A}_{TRIAD}$ is the attitude matrix estimate, $\boldsymbol{r}_1$ and $\boldsymbol{r}_2$ are two reference vectors, and $\boldsymbol{b}_1$ and $\boldsymbol{b}_2$ are two body fixed vectors. The cross-product vectors $\boldsymbol{r}_x$ and $\boldsymbol{b}_x$ can be found using the equation below.

$$\boldsymbol{v}_x = \frac{\boldsymbol{v}_1 \times \boldsymbol{v}_2}{\|\boldsymbol{v}_1 \times \boldsymbol{v}_2\|} \tag{9}$$

Once the attitude matrix is found, it can be converted to a quaternion by treating the attitude matrix as a direction cosine matrix.

3.1.1 Implementation

For this project, the sun and magnetic vectors were chosen. The sun and magnetic body fixed vectors can be determined from magnetometers and sun sensors on the spacecraft. The reference frame vectors are based around Earth and can be determined from magnetic field charts and sun vector charts. To test this project's TRIAD algorithm, data from STK was used to find $\hat{A}_{TRIAD}$ and $\hat{\boldsymbol{q}}_{TRIAD}$ and compare it to "real" $\boldsymbol{q}$, also provided by STK. (reference code in Appendix A). This method was only used for the detumble process and early slew maneuvers.

3.2 Disturbance Modeling

Solar Radiation Pressure

Sunlight can exert a force on the CubeSat's solar panels, causing it to rotate or change its orientation. This force is significant due to the small size of CubeSats. This disturbance torques for solar radiation pressure can be broken up into three causes, absorption and speculative reflection.

Absorption: If solar radiation impinging on a surface is totally absorbent, then the force on the surface will be aligned with the sun vector, and will have magnitude

Speculation Reflection: The force resulting from impingement on a secularly reflective surface is normal to the surface regardless of sun line and is an elastic collision with twice the magnitude of that of an absorbing surface.

Diffuse Reflection: A diffuse layer reflective surface can be considered to be an absorption and radiation uniformly distributed over a hemisphere. The absorption component is aligned with the

sun vector with magnitude given by the one above. The net force resulting from the reflected component is normal to the surface; all tangential components cancel.
Solar torque on the spacecraft is the sum of all forces on all elemental surface's times the radius from the centroid of the surface to the spacecraft center of mass [55].

$$T_s = PAL(1 + q) \tag{10}$$

T_s is the total torque on the spacecraft caused by a surface A, Nm. A is the area of the surface that is projected to the sun line normal in m^2. L is the distance from the centroid of the surface to the center of mass of the spacecraft in meters. q is the reflectance factor where $0 < q < 1$. Spacecraft bodies tend to be reflectors where $q = 0.5$ is a typical spacecraft body and solar panels are more likely to be absorbers i.e., $q = 0.3$ is likely [55].

Atmospheric Drag

Also known as aerodynamic drag, this torque is important even at the altitude where's CubeSats typically operate, there is still a small amount of atmospheric drag. This drag can vary with altitude and can induce torques on the spacecraft [55].

$$D = \frac{1}{2}\rho V^2 C_d A \tag{11}$$

Where D is the drag force which is aligned with the velocity vector and opposite in the sign. ρ is the atmospheric density at the location of the spacecraft in kg/m^3. V is the current spacecraft velocity in the velocity vector in m/s. C_d is the drag coefficient which depends on the shape of the spacecraft, in this case is around 2.5 and is a dimensionless figure [55].

The largest changing factor for determining the drag analysis is the changing atmospheric density which is dependent on factors such as the intensity of solar radiation, time of day, temperature and the altitude. The actual torque applied on the spacecraft is seen in equation (12) [55].

$$T_D = DL \tag{12}$$

Where in this case L is the distance between the center of pressure and the center of gravity of the spacecraft which is determined by the model and the angle of the solar panels as they rotate throughout orbits.

Magnetic Torques

The Earth's magnetic field can interact with the CubeSat's magnetic moment, causing it to experience torques that affect its attitude [55].

$$T_m = NIABsin(\theta) \tag{13}$$

T_m is the magnetic torque in Nm. N is the number of loops in the coil. Where I is the current in the coil measured in amperes and B is the Earth's magnetic field which is measured in Tesla's. θ is the angle between the magnetic field lines and is perpendicular to the coil [55].

Gravitational Torques

Variations in the gravitational field of Earth can lead to torques as the CubeSat moves though different gravitational regions. [54].

$$T_g = \frac{3\mu}{r^3}|I_z - I_y|\theta \tag{14}$$

Where T_g is the gravity-gradient torque expressed in Nm. U is the gravitational parameter which is 398,600.4 km^3/s^2 which is equal to GM. R is the radius from the spacecraft center of mass to the central body center of mass in kilometers. I_z is the moment of inertia of the spacecraft about the z-axis and I_y is the same for the y-axis. Theta is the angle between the spacecraft z-axis and the nadir vector in radians.

3.3 Dynamic Determination

The Kalman filter is a tool that uses both sensor data and system dynamics to estimate a state. This allows the estimation to account for external inputs and previous states, unlike a static determination system. It also provides more accurate results because it uses two estimation methods in tandem. The only problem is that most Kalman filters are for linear systems and are discretized so that the dynamical model has the same time step as the sensor data. The dynamics of a spacecraft move too quickly to fit into a discretized model and are nonlinear. To solve this problem, this MQP uses a continuous discrete extended Kalman filter (CD-EKF). This allows the system dynamics to be computed in a continuous fashion while the sensor readings can still appear at discretized time steps.

3.3.1 Model

To determine and control attitude properly, the control system needs to know 7 variables. These 7 quantities, along with the equations that define them, make up the state of the filter. In addition, for the filter to work, it needs a dynamic model for propagation and a sensor model to update the results of the dynamic model.

$$\boldsymbol{x} = \begin{bmatrix} \omega_1 \\ \omega_2 \\ \omega_3 \\ q_1 \\ q_2 \\ q_3 \\ q_4 \end{bmatrix} \quad , \quad \dot{\boldsymbol{x}} = \begin{bmatrix} \dot{\boldsymbol{\omega}} \\ \dot{\boldsymbol{q}} \end{bmatrix} = \begin{bmatrix} -J^{-1}[\boldsymbol{\omega}\times]\boldsymbol{\omega} + J^{-1}\boldsymbol{L}_c + J^{-1}\boldsymbol{L}_w \\ \frac{1}{2}\Omega(\boldsymbol{\omega})\boldsymbol{q} \end{bmatrix} \tag{15}$$

These two equations make up the true dynamics of the system, or what is otherwise known as the plant. J is the moment of inertia, L_c is the control torque, and L_w is the disturbance torque, as discussed earlier. These equations are based off the true $\boldsymbol{q}$ and $\boldsymbol{\omega}$, two values which can never be known to 100% accuracy, hence why they must be estimated.

$$\boldsymbol{y}_k = \boldsymbol{x}_k + \boldsymbol{v}_k = \begin{bmatrix} \boldsymbol{\omega}_k + \boldsymbol{v}_{k\omega} \\ \hat{\boldsymbol{q}}_{kQUEST} \end{bmatrix} \tag{16}$$

Equation (11), which represents the sensor model in the context of a spacecraft's attitude control system, is discretized due to the nature of how sensor data is collected and processed. Sensors, such as rate gyros and attitude determination systems like QUEST (Quaternion ESTimation), sample physical quantities at discrete time intervals, not continuously. This sampling process inherently discretizes the data, as measurements are only available at specific points in time rather than continuously over time. This process is different that the previously mentioned TRIad process.

Equation (11) is the sensor model. To the filter, this is how new data arrives for the update step. For the actual satellite, the $\boldsymbol{\omega}$ values will come from the rate gyros. However, the quaternion "measurements" will be a quaternion estimates from QUEST. Both values will have noise associated with them that will be elaborated on later.

3.3.2 Determination of Q and R

This section will cover how to get the sensor covariance and dynamic model covariance matrices. The determination of Q and R matrices is a fundamental aspect of designing and implementing a Kalman filter, including the Continuous Discrete Extended Kalman Filter (CD-EKF) used for spacecraft attitude control. These matrices represent the process noise covariance (Q) and measurement noise covariance (R), respectively, and their accurate determination is crucial for the filter's performance in terms of accuracy and stability. The determination of the process noise covariance matrix Q and the measurement noise covariance matrix R is pivotal for the effective application of the Kalman filter, including the CD-EKF used in spacecraft attitude control. Q quantifies the uncertainty in the system dynamics, accounting for unmodeled influences, environmental disturbances, and any assumptions made in the system's mathematical representation. Its accurate estimation often blends theoretical insights, empirical data, and engineering judgment, starting from conservative guesses and refining based on simulation or experimental feedback. On the other hand, R encapsulates the expected inaccuracies and noise in sensor measurements, typically derived from sensor specifications provided by manufacturers, adjusted as necessary through empirical validation under operational conditions. The crux of achieving a well-performing Kalman filter lies in the precise calibration of Q and R. Misestimation can lead to overconfidence in inaccurate estimates or excessive variance, undermining the filter's reliability. Therefore, iterative tuning, leveraging simulations, real-world data, and possibly adaptive methods for real-time adjustments, is essential for maintaining the balance between responsiveness to state changes and resilience against noise and disturbances.

3.3.3 Propagation

$$\dot{\hat{\boldsymbol{x}}} = \begin{bmatrix} \dot{\hat{\boldsymbol{\omega}}} \\ \dot{\hat{\boldsymbol{q}}} \end{bmatrix} = \begin{bmatrix} -J^{-1}[\hat{\boldsymbol{\omega}}\times]\hat{\boldsymbol{\omega}} + J^{-1}\boldsymbol{L}_c + J^{-1}\boldsymbol{L}_w \\ \frac{1}{2}\Omega(\hat{\boldsymbol{\omega}})\hat{\boldsymbol{q}} \end{bmatrix} \tag{17}$$

In the implementation of a CD-EKF we need an understanding and accurately determining the matrices F (state transition matrix) and F (process noise influence matrix) is crucial. The F matrix, derived from the linearization of the system dynamics around the current state estimate, predicts how the state evolves over time without external inputs. It is essentially the Jacobian matrix of the state equations, reflecting how small changes in the state variables

affect the system's evolution. The G matrix, on the other hand, maps the process noise into the state space, showing how uncertainties in the system dynamics influence the state evolution. These matrices are pivotal for the error covariance propagation, ensuring the filter's predictions account for both the system's inherent dynamics and the uncertainty introduced by process noise.

Setting appropriate initial conditions is another critical step, involving the initial state estimate ($\hat{\dot{\boldsymbol{x}}}$) and the initial error covariance matrix (P_0). These parameters establish the filter's starting point, with $\hat{\dot{\boldsymbol{x}}}$ based on prior knowledge or measurements, and P_0 indicating the initial uncertainty. Properly chosen initial conditions are vital for the filter's early performance and its ability to converge to accurate estimates. Moreover, the variables within the CD-EKF framework—such as state variables (angular velocities, quaternions), control inputs (control torques L_c), and disturbances (L_W for disturbance torques)—play significant roles in the filter's operation. The accurate modeling of these variables, alongside the noise covariances Q (process noise covariance) and R (measurement noise covariance), forms the basis for the filter's estimation process. The stability of the filter, particularly in terms of Lyapunov stability, hinges on the proper evolution of the error covariance matrix (P). The equation (17) describes how P changes over time, incorporating both the prediction of the system's future state and the impact of process noise. Ensuring that this propagation does not lead to an increase in the estimation error is essential for maintaining the filter's reliability and effectiveness. Achieving this stability involves a careful balance of system modeling, parameter tuning, and leveraging insights from Lyapunov's theory to guarantee that the filter remains stable, and the estimation errors do not grow unbounded over time.

Equation (13) represents the model used for dynamic propagation of the state. Because the equations of motion change rapidly, the equations are solved on very small-time steps using an ode solver. The result is a better estimate of the state than would come from using the same time step as the sensor model. For this process L_c and L_w remain constant and will only change after the update step.

The error covariance matrix must be calculated using several shortcuts due to its massive computational expense. It is assumed that P is constant between measurement time steps and the Q is a scalar. With these assumptions, the variables in the $\dot{P}$ are all constants between measurement time steps.

3.3.4 Calculating Gain

The gain in a Kalman filter, particularly in the context of a CD-EKF, plays a pivotal role in determining the filter's performance. This gain, often denoted as K, essentially dictates the balance between reliance on new sensor data and trust in predictions based on the system's dynamics. The calibration of K is critical; it influences how the filter integrates incoming measurements with the predicted state to produce an updated estimate.

The gain is calculated in a way that minimizes the estimation error covariance, reflecting the filter's confidence in the accuracy of the model predictions versus the measurements. A high gain indicates greater trust in the sensor data, compelling the filter to adjust its estimates more significantly in response to new measurements. Conversely, a lower gain suggests more confidence in the model's dynamics, leading to more conservative updates based on new data.

Adjusting the Kalman gain is a delicate process. If the gain is set too high, the filter may become overly responsive to measurement noise, potentially leading to erratic estimates. If set too low, the filter might ignore valuable information in the measurements, resulting in sluggish response to actual changes in the system's state. Thus, the determination of the Kalman gain is a

crucial aspect of filter design, requiring a nuanced understanding of both the system dynamics and the characteristics of the sensor data to achieve an optimal balance that ensures accurate, stable, and responsive state estimation.

$$K_k = P_k^- H_k^T [H_k P_k^- H_k^T + R_k]^{-1} \tag{18}$$

Equation (18) defines the calculation of the Kalman gain K_k, which is central to the Kalman filter's update step. This equation finely tunes the balance between the predictions based on the system's dynamics and the latest measurements. Here, P_k represents the a priori error covariance matrix before incorporating the measurement at time step k, and H_k is the measurement matrix that maps the state space into the measurement space at the same time step. R_k is the measurement noise covariance matrix, encapsulating the expected noise in the measurements. The matrix H_k is crucial as it directly influences how the state estimates are updated with new measurements. Finding the appropriate form of H_k often involves understanding the relationship between the state variables and the measurements, which can be system-specific and may require linearization in the case of nonlinear systems. Details on deriving H_k for a particular system are typically elaborated in the appendix or a dedicated section of documentation, where the focus is on the mathematical derivation and its justification based on the system's measurement model. Similarly, the source and determination of R_k are critical for accurately capturing the measurement noise characteristics. R_k usually comes from empirical data, sensor specifications, or a combination of both, reflecting the variance and covariance of the noise in sensor readings. This matrix is pivotal for weighting the measurements during the update process: a larger R_k implies less trust in the measurements due to higher noise levels, whereas a smaller R_k indicates more reliable sensor data. The appendix often provides a detailed rationale for the chosen R_k values, including the methods used for its estimation, whether through direct measurement, analysis of sensor specifications, or statistical methods applied to historical data.

In summary, Equation (18) not only highlights the mechanism through which the Kalman filter integrates new information but also underscores the importance of accurately defining H_k and R_k. These matrices are essential for the effective application of the filter, requiring detailed attention to both the theoretical underpinnings and practical considerations of their determination.

After many time steps of propagating, a new sensor value will arrive, and the filter will be discretized to the measurement time step. At this point, P^- is calculated from $\dot{P}$ in the propagation. R represents the measurement noise covariance. The covariance of each of the q values is calculated during the QUEST estimation and the covariance of each ω is determined from the sensor manufacturer. Additional information on the H matrix can be found in Appendix C.

3.3.5 Update Step

$$\hat{\boldsymbol{x}}_k^+ = \hat{\boldsymbol{x}}_k^- + K_k[\boldsymbol{y}_k - \hat{\boldsymbol{x}}_k^-] \tag{19}$$

$$P_k^+ = [I - K_k H_k] P_k^- \tag{20}$$

The update step puts all the final components together. The $\widehat{\mathbf{x}_\mathbf{k}^+}$ is the final and most accurate estimate. This value goes into the controller. Further iterations use the $\widehat{\boldsymbol{x}_\boldsymbol{k}^+}$ and P^+ values from the last iteration and plug them back into the propagation stage. At this point, the controller and the disturbance models will give the propagation step a new $\boldsymbol{L_c}$ and $\boldsymbol{L_w}$.

3.4 Detumble Control

In the initial phase of a CubeSat's deployment into orbit, the spacecraft often finds itself in a state of uncontrolled spin or tumble, a condition that can significantly impair its operational capabilities and mission objectives. Detumbling, therefore, becomes a critical first step in the stabilization process, allowing the spacecraft to transition from an erratic spin to a stable attitude control mode. This paper focuses on the implementation of Mode 0 detumbling of the spacecraft using magnetorquers, which are magnetic coils that leverage the Earth's magnetic field to generate torques to counteract the spin.

Detumbling is essential for several reasons:

Communication Efficiency: Communication signals, especially those in the microwave band, are often polarized. A tumbling spacecraft can disrupt the alignment between its antennas and the ground station, leading to significant signal degradation or loss. By achieving a stable orientation, the CubeSat can maintain a consistent and reliable communication link, ensuring the successful transmission of data back to Earth.

Power Generation: CubeSats typically rely on solar panels for power. A tumbling motion can prevent these panels from being optimally oriented towards the Sun, resulting in inefficient power generation and potentially compromising POGSat's energy budget.

Orbital Maneuvering: For missions that require orbital adjustments or rendezvous with other objects, a stable platform is essential. A tumbling spacecraft lacks the controlled orientation needed for executing such maneuvers accurately.

Thermal Management: The orientation of the spacecraft affects its thermal profile by exposing different surfaces to the Sun. Uncontrolled tumbling can lead to thermal imbalances, risking damage to sensitive components through overheating or excessive cooling.

The detumble process using magnetorquers involves the measurement of the spacecraft's angular velocity through onboard sensors, followed by the application of corrective magnetic torques to gradually reduce this velocity. This approach is favored for its simplicity, low power consumption, and the absence of expendable resources, making it particularly suitable for the size, weight, and power constraints of CubeSat missions. This section will delve into the technical details of the detumble strategy, outlining the design, implementation, and operational

considerations for effectively stabilizing the spacecraft using magnetorquers, setting the stage for subsequent mission phases.

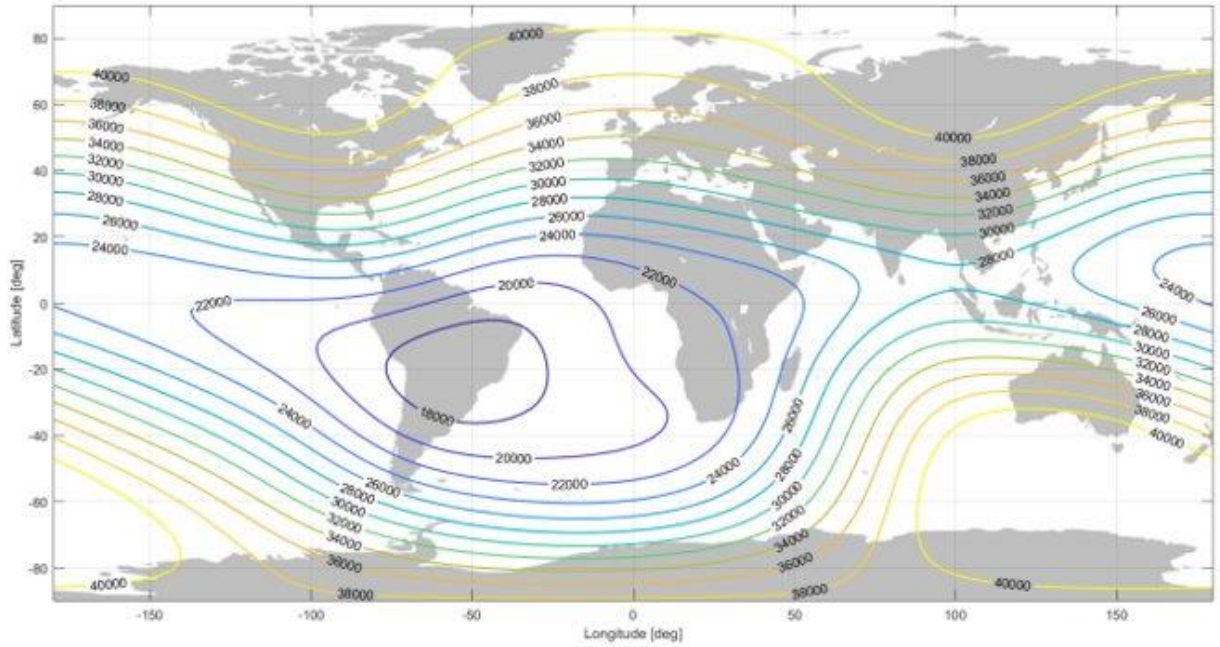

Figure 17 : IGRF 10th Magnetic Field Map [63]

The IGRF 10th Magnetic Field Map is seen above in the figure, where it is the strength of the magnetic field. The strength of the magnetic field is determined by several factors such as longitudinal and latitudinal values alongside altitude. Given those factors we can estimate the strength of the magnetic field which in terns helps us to create a control system based on magnetorquers.

B-Dot Control law, B-Dot Control: The term $\dot{\boldsymbol{B}}$ refers to the rate of change of the Earth's magnetic field as experienced by the CubeSat. When the satellite rotates, this is the magnetic field vector it measures changes over time. This change is captured by $\dot{\boldsymbol{B}}$.

$$L \quad = -k\dot{\boldsymbol{B}} \tag{21}$$

$-k\dot{\boldsymbol{B}}$ generates magnetic torques opposing the rate of change by the Earth's magnetic field. This induces a force that resists the CubeSat rotation. Coefficient k represents the strength and orientation of the magnetic dipole moment of the magnetorquers.

Magnetic Field Vector & K

Magnetic field vector where $\dot{\boldsymbol{R}} \ll \dot{\boldsymbol{B}}$

$$\dot{\boldsymbol{B}} = A\dot{\boldsymbol{R}} - \omega \times \boldsymbol{B} \tag{22}$$

Where T_{orb} is the orbital period (s), ξ_m is inclination of spacecraft relative to geomagnetic equatorial plane and J_{min} is the minimum principal moment of inertia.

$$k = \frac{4\pi}{Y_{orb}}(1 + sin(\xi_m)J_{min}$$

(23)

Control Torque

For the control torque, the equation uses *k* which is defined above, it's a constant. **B** is the real magnetic field from IGRF (13th), ω is the measured rotational velocity. The control law is basically the main goal of the ADCS system as it is what defines what the actuators need to do.

$$\boldsymbol{L} = \frac{k}{\|\boldsymbol{B}\|}(\boldsymbol{\omega} \times \boldsymbol{b}) \times \boldsymbol{B} = k(\boldsymbol{\omega} \times \boldsymbol{b}) \times \boldsymbol{b}$$

(24)

Magnetic Dipole Moment

The magnetic dipole moment on a CubeSat is essentially a vector quantity that represents the strength and orientation of the CubeSat's magnetic field. Where $b=B/\|B\|$, ω is the angular velocity and k is positive scalar gain. Setting Equation (25) to Equation (26) we can find the strength of $\boldsymbol{b}_{true}$. $\boldsymbol{b}$ is the measured magnetic field onboard the S/C

$$\boldsymbol{m} = \frac{k}{\|\boldsymbol{B}\|}\omega \times \boldsymbol{b}$$

(25)

$$\boldsymbol{m} = -\frac{k}{\|\boldsymbol{B}\|}\dot{\boldsymbol{B}}$$

(26)

Current MATLAB Script for mode 0 (Detumble)

Inertia matrix is based on an Example 12U CubeSat. Based on a polar orbit with an 89-degree inclination (which should be worst case in terms of control ability). Takes into account changing location and magnetic field and utilizes IGRF model 13th. Implemented 30 min wait period for activation of mode 0; this is because one of the requirements of a CubeSat is to be inactive from deployment to 30mins afterwards. For the detumble threshold it is defined as equal to or less than 0.05 degree/sec. Initial Rotation is 15 degree/second from deployment (estimate from the structures half of this Major Qualifying Project is 10 deg/sec).

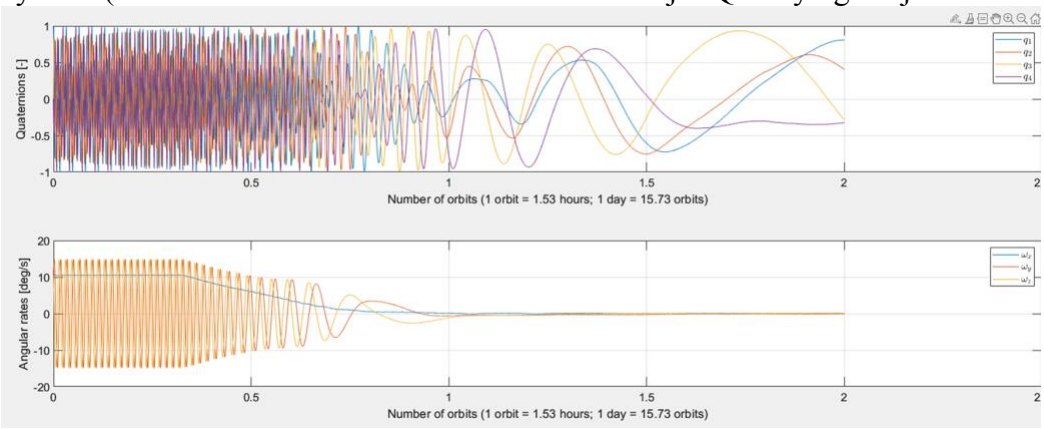

Figure 18 : Quaternions and Angular Rates for the CubeSat during detumble.

As we can see in the figure, the quaternions look to be correct, and in this case, we are using “corrupted quaternions” as we are not implementing a EKF for mode 0 and the sensors have natural noise which is estimated using a simple gaussian noise generator built into MATLAB. And below the quaternions is our angular rates of the spacecraft and once that hits 0.05 degrees/sec it has detumbled in this scenario which is gone into more detail later on.

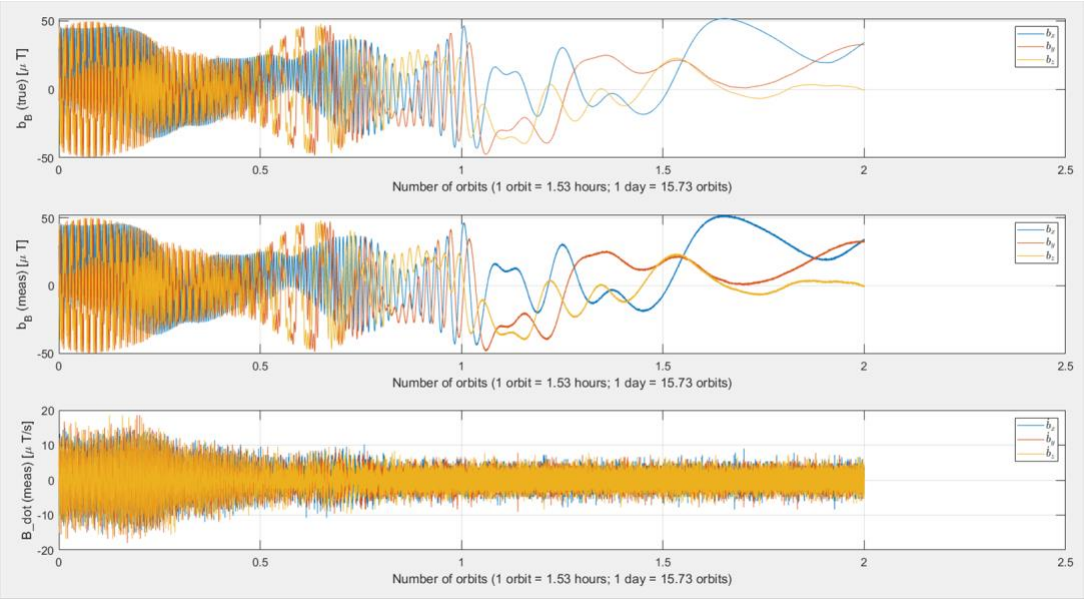

Figure 19 : B-dot control law and magnetic field strength.

Above in the figure we can see the “true” and measured magnetic field strength observed by the CubeSat over time and at the bottom is the output of our B-dot control law which is the one that controls the output of each of our three magnetorquers which apply the rotational torque to control the spacecraft.

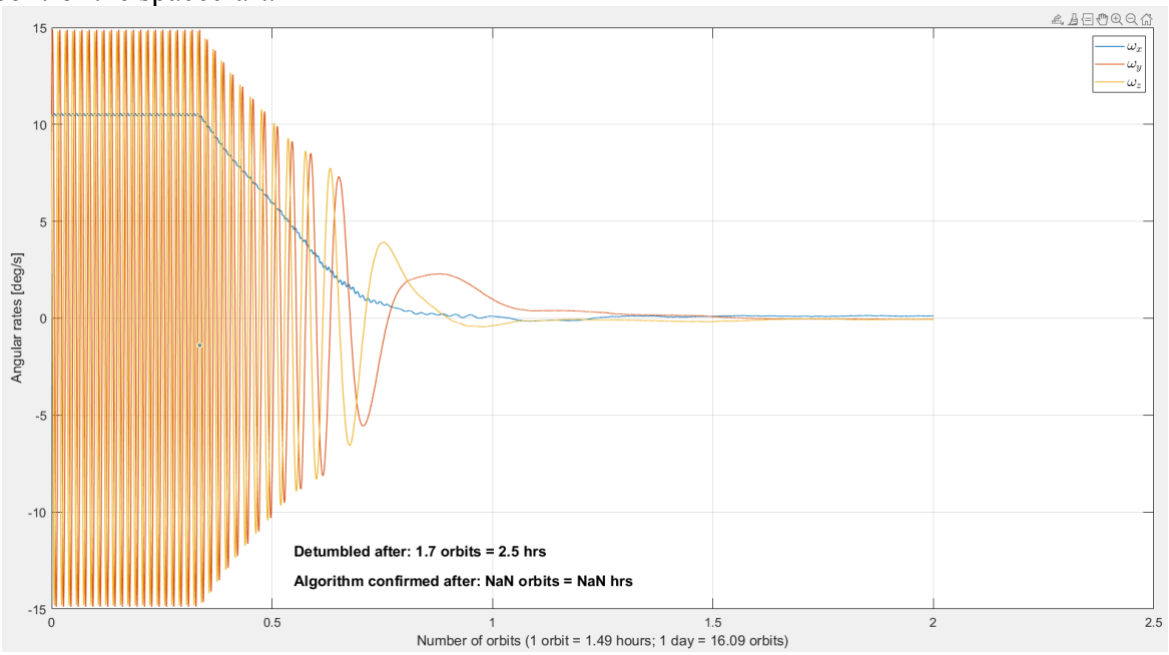

Figure 20 : Detumble Time Estimation Graph.

The observed angular rates of the spacecraft reduce to zero, indicating the successful operation of the detumbling process. The relevant script segment monitors angular velocities and confirms detumbling completion when they fall below the designated threshold. This state was achieved after approximately 1.7 orbits, or 2.5 hours, which aligns with our operational requirements. Consequently, we can affirm that the detumbling system functions effectively within the expected timeframe.

3.5 Mission Control

After detumble, the solar arrays will deploy, thus changing the moment of inertia. At this point, the satellite needs a different control system. This new control system will be able to point in any direction needed, based on the user input of $\boldsymbol{q_{desire}}$, without straining the power system.

For the remainder of the phases, the ADC system will follow the block diagram shown. The precise dynamics of the spacecraft cannot be known by the controller and are represented by a black box. In this model, sensors will read the $\boldsymbol{\omega}$ values, while the quaternion is estimated by a static estimator. These values are denoted as $\hat{\boldsymbol{q}}$ and $\hat{\boldsymbol{\omega}}$ because they are estimates and have noise associated with them. These values are then sent to the dynamic filter. The dynamic filter will send estimates to the controller. With these estimates, the controller can calculate the torque needed to stabilize the spacecraft. The filter acknowledges this torque and uses it to propagate the next estimates for **q** and **ω**. During the mission, there will be several different ADCS objectives. These are determined by mission phase and mission requirements.

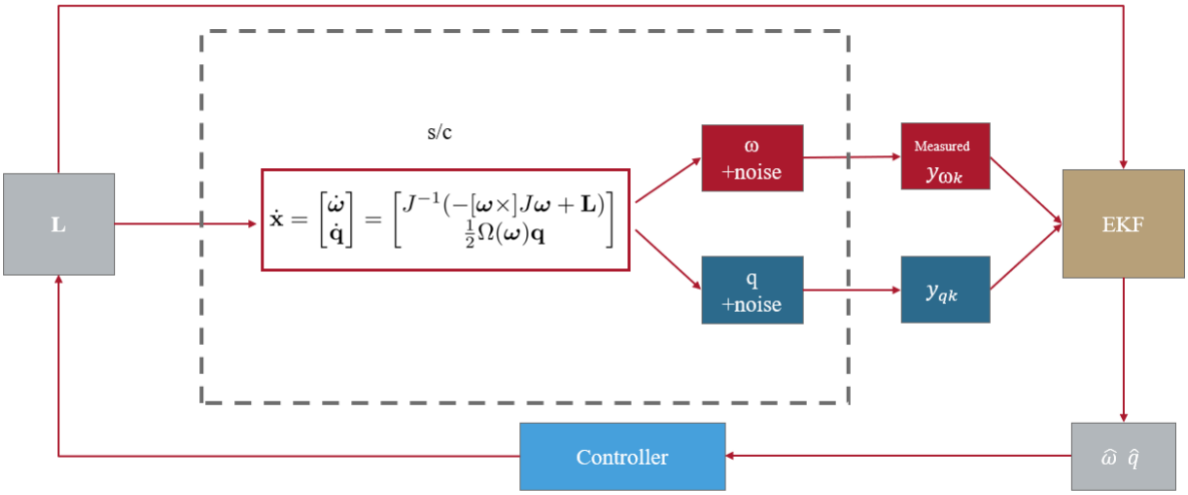

Figure 21: Attitude Determination and Control System basic block diagram.

3.2.5 Control Design

This control system will be broken into several sections. A desired attitude is selected by the spacecraft operator and measured attitude is used to determine the attitude error. Furthermore, the disturbance torques will be factored in using models above.

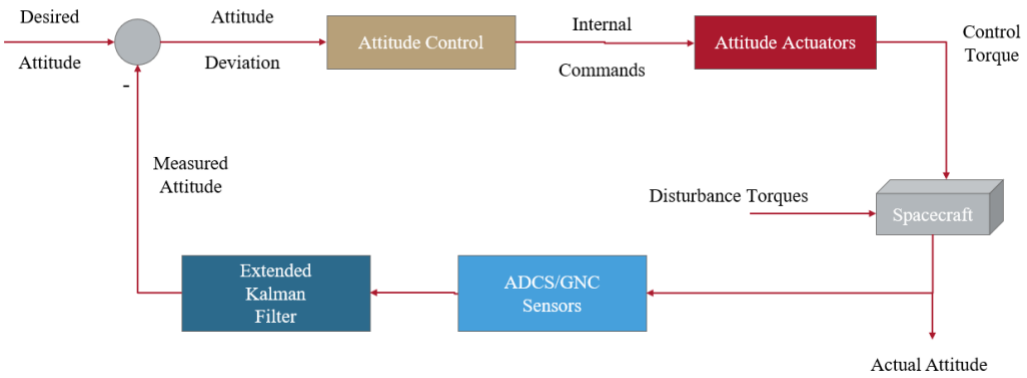

Figure 22 : Control System Block Diagram.

Above in Figure 22, the general ADCS system flow diagram can be seen. The input of the system is the desired attitude. Using computations, the attitude error $\delta\boldsymbol{q}$ is found, which goes into the controller. From here the controller determines the needed torque in each axis and sends commands to the attitude actuation system. In this case the actuators are made up of a magnetorquer on each axis, and a current is applied to cause movement.

The controller determines control torque from various equations. For this MQP, the selected equations are from the Fundamentals of Spacecraft Attitude Determination and Control textbook [55]. The book provides four options for controlling the spacecraft, however only two of them are for nonlinear systems. Each of them relies on the same inputs but produces a slightly different control torque from those inputs. Each of these equations requires an $\boldsymbol{\omega}$ value, two k values, and the $\delta\boldsymbol{q}$ error quaternion value. The error quaternion can be calculated using the equation below, with the current $\boldsymbol{q}$ and $\boldsymbol{q}_{desired}$ values.

$$\delta\boldsymbol{q} = \begin{bmatrix} \delta\boldsymbol{q}_{\boldsymbol{1:3}} \\ \delta q_4 \end{bmatrix} = \boldsymbol{q} \otimes \boldsymbol{q}_d^{-1} \tag{27}$$

The difference between these control laws is in aggression. The gains can be selected to change the aggression of each controller, however, the second controller listed here is generally more aggressive and returns to $\boldsymbol{q}_d$ the fastest. Because POGSat's payload requires very stable pointing for the science phase, the second more aggressive controller was chosen. It should be noted that in practice, the controller will use $\hat{\boldsymbol{\omega}}$ because the true $\boldsymbol{\omega}$ cannot be known.

$$\boldsymbol{L}_c = -k_p \delta\boldsymbol{q}_{\boldsymbol{1:3}} - k_d\left(1 \pm \delta\boldsymbol{q}_{\boldsymbol{1:3}}^{\boldsymbol{T}} \delta\boldsymbol{q}_{\boldsymbol{1:3}}\right)\boldsymbol{\omega} \tag{28}$$

$$\boldsymbol{L}_c = -k_p sign(\delta q_4)\delta\boldsymbol{q}_{\boldsymbol{1:3}} - k_d\left(1 \pm \delta\boldsymbol{q}_{\boldsymbol{1:3}}^{\boldsymbol{T}} \delta\boldsymbol{q}_{\boldsymbol{1:3}}\right)\boldsymbol{\omega} \tag{29}$$

3.2.5 Mission Control Implementation

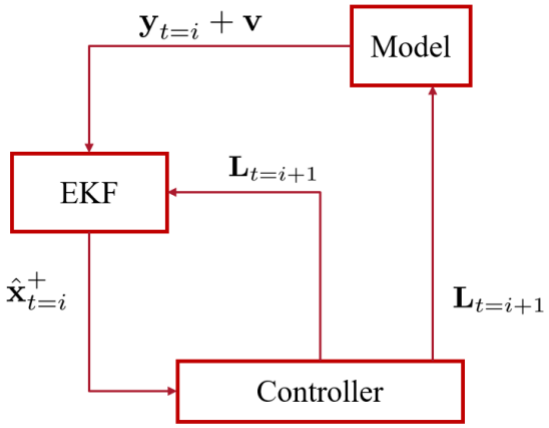

Figure 23: Basic Simulink design of the scientific phase of the ADCS.

The current model for the ADC system is a combination of MATLAB and STK. STK is used to generate the initial and desired $\boldsymbol{x}$, while MATLAB is used for the computations. The implementation goes according to the diagram. It starts with the model using the equations of motion to simulate theoretical spacecraft motion.

$$\dot{\boldsymbol{x}} = \begin{bmatrix} \dot{\boldsymbol{\omega}} \\ \dot{\boldsymbol{q}} \end{bmatrix} = \begin{bmatrix} -J^{-1}[\boldsymbol{\omega}\times]\boldsymbol{\omega} + J^{-1}\boldsymbol{L}_c + J^{-1}\boldsymbol{L}_w \\ \frac{1}{2}\Omega(\boldsymbol{\omega})\boldsymbol{q} \end{bmatrix} \tag{30}$$

These equations are similar to the dynamic estimations of the EKK; however, they are not based on estimates. The model approximates what would happen in practice and then sends a "sensor" value to the EKF. Currently controller uses a .2s time step, however, the model and EKF can't run at this speed because of the nonlinear nature of the system. From here the EKF computes an estimate of the state and the controller determines the torque required to move to the correct $\boldsymbol{q_d}$ and set $\boldsymbol{\omega}$ to 0. The final action of the ADC system is to send the $\boldsymbol{L_c}$ vector back into both the model and the EKF. This ADC system was tested using MATLAB.

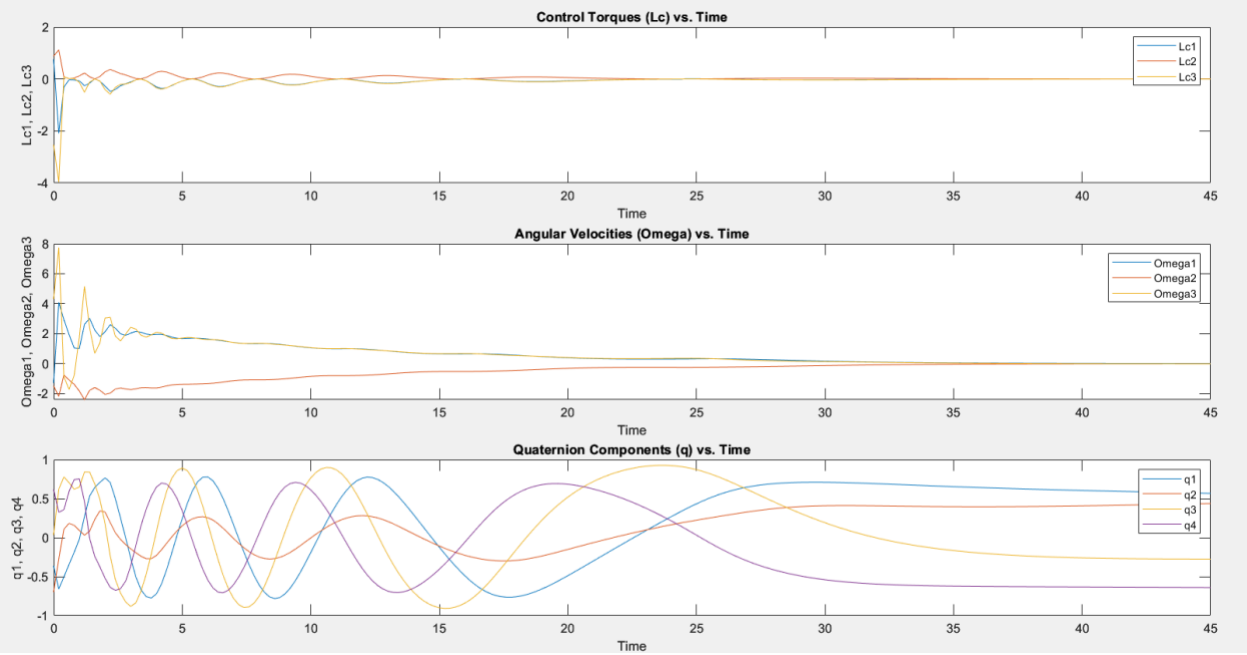

Figure 24: The main control system working in MATLAB.

As can be seen, this controller and EKF combination works. By changing the gains, and adding finer implementations of the covariance matrices, the desired torque can be tuned. Currently the magnetorquers are not equipped to handle torques of 4 Nm, however this can be tuned to be more realistic.

3.3 Sun Sensor Sun-System

The Sun sensor's primary function is to detect the position of the sun relative to the CubeSat's orientation in space. This information is essential for determining the satellite's attitude (orientation) accurately. By knowing the position of the sun, the ADCS can calculate the CubeSat's orientation relative to the sun, which is vital for various operations such as power generation (by aligning solar panels), communication (by pointing antennas), and thermal management (by controlling the distribution of heat). In this mission we need to align solar panels and may need to orient antennas in case of failure.

Sun sensors usually consist of photodiodes or other light-sensitive devices arranged in an array or other configurations to detect the intensity and direction of sunlight. Based on the readings from these sensors, algorithms within the ADCS software can determine the satellite's attitude relative to the sun.

There are two main types of sun sensors, coarse and fine types. Coarse is simpler and detects strength of light in any direction. The fine sun sensor is akin to a camera sensor in which it can detect light on two axes though a hole which helps to determine the direction the sun is coming from. The system of the Sun Sensors is made up of 5 coarse sun sensors and 1 fine sun sensor. The overall goal of the system to determine the inertial frame sun vector. Or in other words the vector (direction) in which the sun is coming from which can then determine the orientation of the CubeSat. However, there are several steps to get to the output.

To determine the incidence angles of sensors 1 & 2 you need to know the raw sensor data. The data is expected in the voltage output of the sensors which is denoted V and the initial

being V0. This computation is done using all pairs of sun sensors that share a side. This determines the alpha angles for multiple pairs of sun sensors which then in turn gives the calculated coarse sun sensors.

$$V_1 = V_{01}\sin(\alpha_1) \tag{31}$$

$$V_2 = V_{02}\sin(\alpha_2) \tag{32}$$

These identities can be related using equations (31) and (32).

$$\begin{bmatrix}\sin(\alpha_1)\\ \sin(\alpha_2)\end{bmatrix} = \begin{bmatrix}\frac{V_1}{V_{01}}\\ \frac{V_2}{V_{02}}\end{bmatrix} \tag{33}$$

Using equation (33) the incidence angles can be found for the sun for each pair of sensors that detect light. Sensors that record low levels of light are removed from the computational process. This algorithm removes "false suns" which can be a cause from things such as the reflection from the earth. Using the computed alpha values the sun sensor in the sensors frame (also denoted $\vec{S}_{sensor}$) can be found using equation (34).

$$\vec{S}_{sensor} = [1\tan(\alpha_1)/\tan(\alpha_2)\tan(\alpha_1)]^T = \begin{bmatrix}S_\phi\\ S_\theta\\ S_\psi\end{bmatrix} \tag{34}$$

The sun vector in the body frame also denoted ($\vec{S}_{computed}$) which is the sun vector in the body frame of the spacecraft.

$$\vec{S}_{computed} = \frac{[1\tan(\alpha_1)/\tan(\alpha_2)\tan(\alpha_1)]^T}{\sqrt{\vec{S}_{sensor}{}^T \cdot \vec{S}_{sensor}}} \tag{35}$$

In the sun sensor sub-system, we are using five coarse sun sensors and one fine sun sensor. So let us now talk about the fine sun sensor system. The reason to only use one fine sun sensor is due to the added expense and complexity of multiple fine sun sensors. A system with just coarse sun sensors is less precise. However, as the goal of the ADCS is to have the z-axis always pointing nadir-in we can place the fine sun sensor in the optimal location to min-max our performance to cost and complexity in the sensors. When used in this system it gives us the accuracy that was needed. The only time in which sensors that are in an unknown configuration is during the detumble mode. In the detumble mode accuracy is less important and thus does not need higher precision.

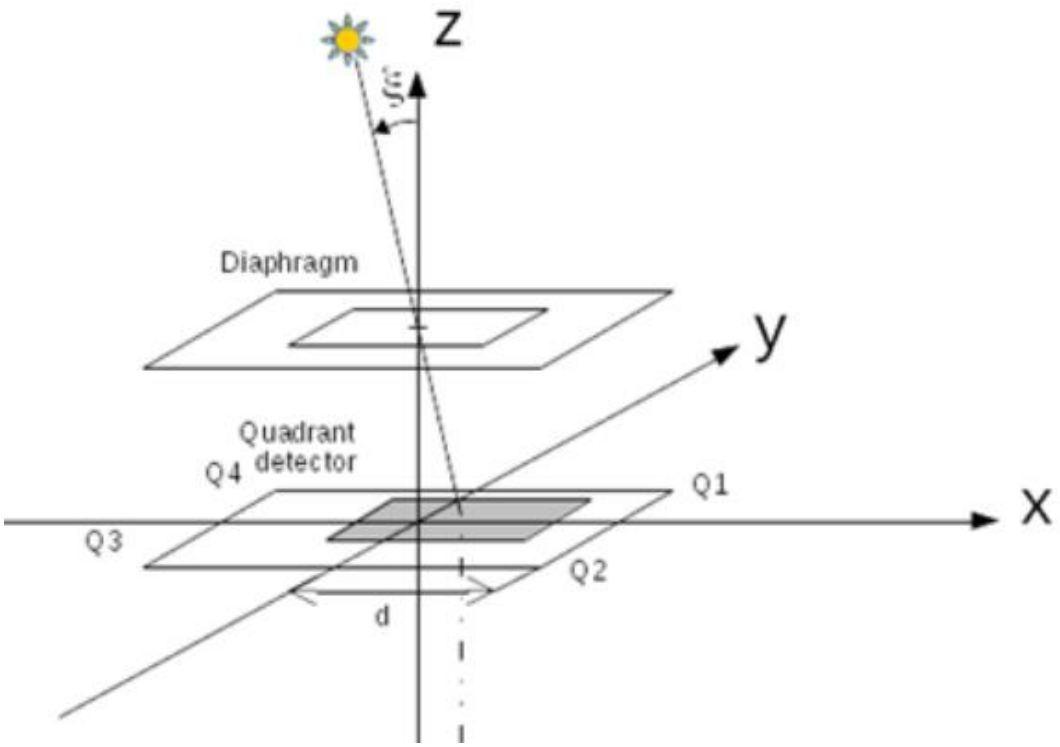

Figure 25: Fine Sun Sensor Diagram, side view (Courtesy of satsearch) [67].

As shown above in Figure 25, the diagram of the fine sun sensor can be seen. The fine sun sensor works similarly to that of a camera sensor. However, there is a light filter known as the diaphragm which is effectively a light hole. Using the pinhole the sensor can determine where the strongest light is hitting it by quadrant and then by the coordinates of y and x of that quadrant. With this information a rough sun vector [67].

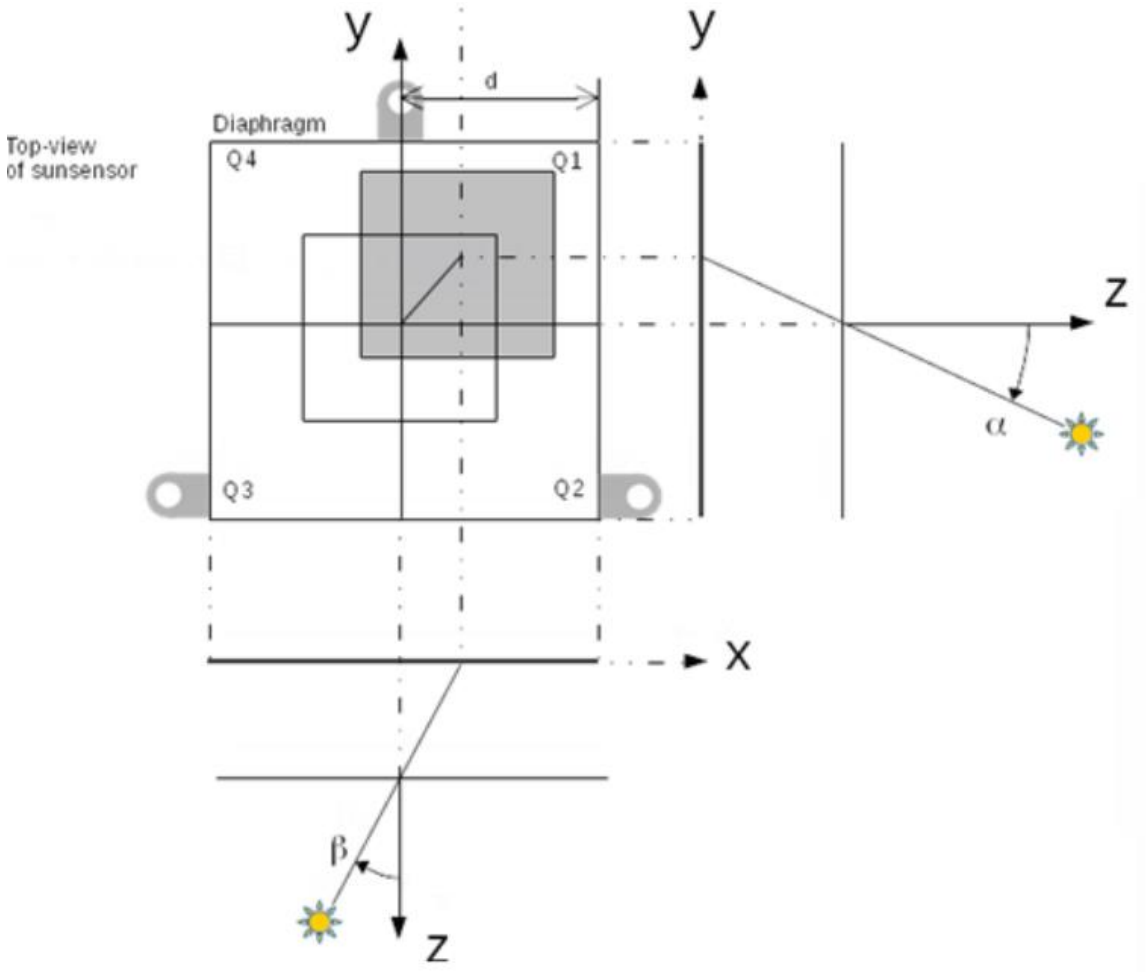

Figure 26: Top view of the Fine Sun-Sensor (Courtesy of satsearch) [67].

Now let's divulge into a simplified overview of the steps for determining the sensor sun vector for a fine sun sensor. The steps are to first find the sun vector for the sensor then the body frame and lastly inertial frame [67].

(36)

$$\vec{S}_{sensor} = [cos\,\alpha\, cos(\beta)\,, cos(\alpha)\, sin(\beta)\,, sin(\alpha)]$$

After computing the sun vector in the sensor frame to go to the body frame you must apply a rational matrix dependent on the axis the sun sensor is lying on. θ is representative of the angle to the plane the sensor is on [67].

(37)

$$R_x(\theta) = \begin{bmatrix} 1 & 0 & 0 \\ 0 & cos\,(\theta) & -sin\,(\theta) \\ 0 & sin\,(\theta) & cos\,(\theta) \end{bmatrix}$$

(38)

$$R_y(\theta) = \begin{bmatrix} cos\,(\theta) & 0 & sin\,(\theta) \\ 0 & 1 & 0 \\ -sin\,(\theta) & 0 & cos\,(\theta) \end{bmatrix}$$

(39)

$$R_z(\theta) = \begin{bmatrix} \cos(\theta) & -\sin(\theta) & 0 \\ \sin(\theta) & \cos(\theta) & 0 \\ 0 & 0 & 1 \end{bmatrix}$$

After computing the rotational matrices, you simply cross your rotation matrix with the computed sensor frame sun vector.

(40)

$$\vec{S}_{body} = R \cdot \vec{S}_{sensor}$$

The sun vector in the body frame is a fourth of the important part of determining the exact attitude with the ADCS system [67].

3.4 Magnetometer System

The magnetometer system emerges as a cornerstone component within a CubeSat's Attitude Determination and Control System (ADCS), instrumental for its precision and reliability in space missions. At its core, the magnetometer processes a fusion of raw sensor data and precise location information, courtesy of the ADCS's GPS capabilities, to accurately map the local magnetic field and ascertain the spacecraft's orientation relative to this field. This dual-input system enables the determination of the CubeSat's positioning not only in its immediate vicinity but also in relation to broader celestial coordinates, aligning the spacecraft's body frame and inertial frame with the local geomagnetic contours. The outputs—critical insights into the local magnetic environment and the CubeSat's orientation therein—are pivotal for navigational adjustments and operational decision-making. Moreover, in the event of ADCS component failures, the magnetometer's capability to independently compute orientation offers fail-safe, ensuring the mission's continued viability. Thus, the magnetometer stands as both a fundamental tool for daily operations and a critical backup system, underscoring its indispensability in the complex orchestration of CubeSat functionalities. To clear up each of the vectors it is important to note that $\vec{B}_{body} = \vec{B}_{measured}$ and $\vec{B}_{inertial} = \vec{B}_{true}$ are equal to each other. In this case, τ is the difference angle for each axis.

(41)

$$\vec{B}_m \cdot \vec{B}_t = |\vec{B}_m||\vec{B}_t|\cos(\tau)$$

(42)

$$\tau = cos^{-1}\left(\frac{\vec{B}_m \cdot \vec{B}_t}{|\vec{B}_m||\vec{B}_t|}\right)$$

The above equation does have continuity issues however, this is resolved as the internal body frame is less important in the overall ADCS system. For the backup calculation in MATLAB the encompass function is used in each axis. This computation is used for the detumble system exclusively.

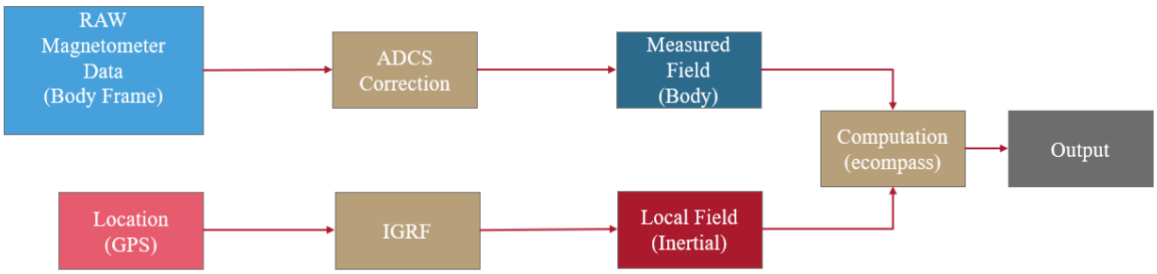

Figure 27: The block diagram for the magnetometer sub-system.

As seen in Figure 27, the magnetometers have several outputs, one is the all-important body frame field vector which is observed by the spacecraft which is compared to the true magnetic field. However, for the detumble section, the ADCS system is in a much simpler mode in which it uses the difference using the above process to determine orientation. If the detumble mode realizes it is not accurate enough it simply uses the ADCS system sensors like that in the science mode which is substantially more accurate.

3.5 Constant Facing Maneuvers

One of the requirements of the payload is to have the z-axis of the CubeSat always pointing Nadir-in during the length of the orbit while the x-axis is facing the velocity vector. This was to ensure the highest capability of payload this section of the ADCS had to be met.

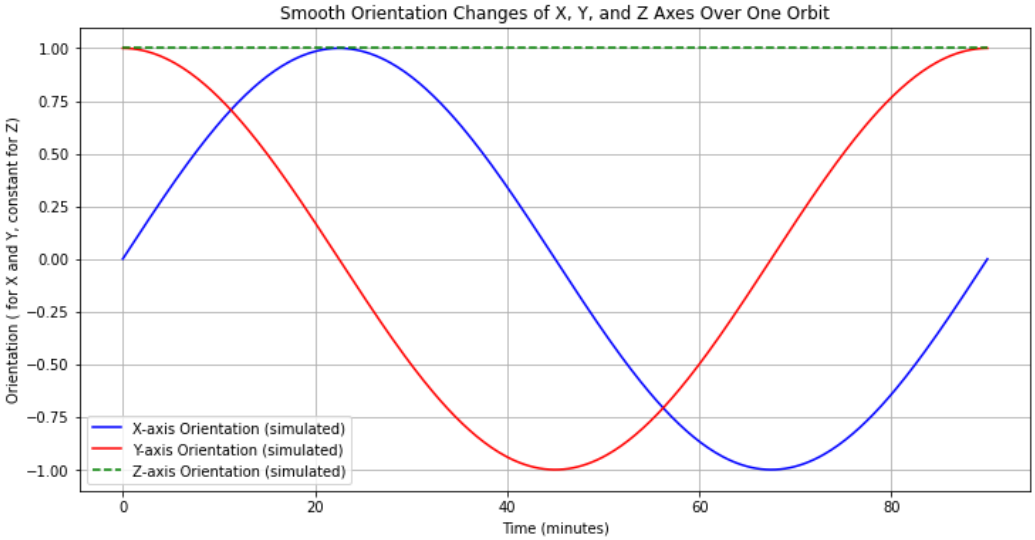

Figure 28: Orientation Changes for Science Mode of ADCS. Modeled in Python.

Above in Figure 28, is the orientation graph for each of the axis of the spacecraft for the duration of one orbit (approximately 90mins). It can be observed that the orientation is described as -1 through 1 which was due to the process of simplifying the computational process and at the real output of the system is in the expected radians. As the z-axis is always pointing nadir-in it does not change from its orientation while the x and y axis do change during the orbital period, which is expected.

3.6 Slew Maneuvers

Slew Maneuvers are the name of the change of orientation maneuvers of a spacecraft. It is an estimation of how fast the spacecraft will be able to change orientation of a specified slew distance and in which time it would take. Ideally a spacecraft would take no time to reorient. However, this is impractical and could be damaging and thus there needs to be a balance between strength of actuators and damage. In the case of POGSat, the system is overbuilt and thus does not use the majority of its powers in slew maneuvers, but the table represents full power and full pointing precision.

Table 5: Slew Table

Slew Distance	**Slew Time [s]**
0"–0.05"	0
>0.05" to 15"	1
15"–25"	1.2
>25" to 3°	6
>3° to 180°	25

This slew table above shows that the CubeSat is easily able to orient whichever way it needs to regardless of the situation that it finds itself in. As a result, the controller and the magnetorquers are well suited for the environment and design of the CubeSat. Thus, we have struck the balance point for how strong the actuators need to be for the given inertia of worst case and worst-case disturbance torques on the spacecraft.

3.7 Conclusions on the ADCS System

The ADCS system initially needed to have an accuracy of at least 350 arc seconds or 0.1 degrees but it was determined for the needed accuracy for the payload to be at least 180 arc seconds or 0.05 degrees in each axis to ensure the highest degree of accuracy for both the ADCS but also the main payload as for the integrity of the mission is paramount to know the orientation of the CubeSat at the time of data logging. After the process was completed simulating the ADCS system, a physical system was built for demonstration with an accuracy of 5 arc seconds, which is more accurate than was specified for the minimum. This was verified using several processes. The Detumble system had a goal of detumbling within the specified two orbit range which was achieved at 1.7 orbits in the worst-case scenario. And lastly, the slew maneuvers were much faster than what was needed and thus also fit within the use case of the entire CubeSat system. Therefore, we can conclude that the ADCS system would be fully up and operational.

4 Power

The power system is a crucial component of the spacecraft that handles the generation, conditioning, and distribution of power to the satellite and its subsystems. This MQP will be using solar panels for generation and batteries for power storage, for when the satellite is in eclipse. Solar panels are composed of photovoltaic solar cells that transform solar radiation into electrical energy. This generated energy is stored in the battery or sent to satellite systems, according to the power distribution design. Alternative power generation methods were investigated, but the size and complexity of other options made the alternatives infeasible. Due to the very low altitude the satellite for both orbits, it is expected that the satellite will be in very frequent, short eclipses. Below is the power budget for each phase of the mission.

Table 6: Power budgets for each phase of the mission.

Power Consumer	Phase 1	Phase 2	Phase3
Propulsion	100W	100W	0W
ADCS	2W	2W	2W
Computer	2W	2W	2W
Comms	1W	1W	1W
Total	105W	105W	5W

4.1 Solar Array Design

Due to the nature of the payload, the satellite cannot point to increase power production. The satellite must also maintain a constant center of mass. Thus, the best design is one that move symmetrically to capture the sun and maintain center of mass of the spacecraft. This mission will be using the EnduroSat 3U CubeSat solar panels.

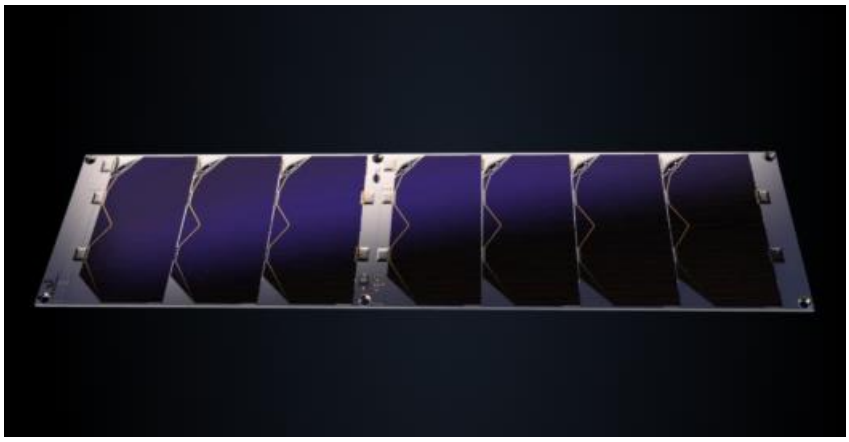

Figure 29: An EnduroSat 3U solar panel array [69].

These solar panels are about the highest efficiency possible for flight ready panels at 29.5% [69]. They also have a yearly degradation value of 0.017 and distinct flight heritage [70]. The sun sensors directly on these panels easily facilitate the need for them to rotate. These panels also have a structure factor of 11%, making their effective area 11% smaller.

4.1.1 Sun Vector

The sun vector over the course of a year is ultimately what defines the orientation and arrangement of the solar arrays. Both orbits of the mission are extremely high inclination, which gives them about the same orbital characteristics over the course of a year. Vector analysis of one will suffice for the other. Over the course of a year, there are two general patterns that emerge in the solar vector.

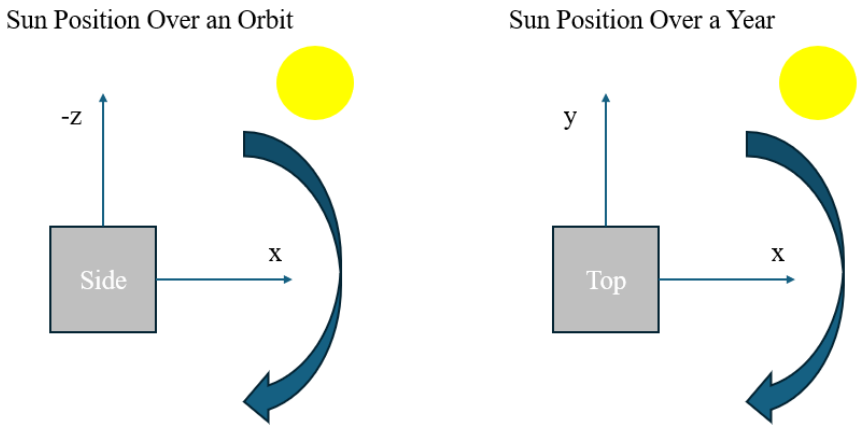

Figure 30: The sun position over the course of an orbit and a year.

As seen in Figure 30, the solar vector over an orbit moves up and down the x-z axis while over a year the sun vector rotates around the x-y axis. This represents the first pattern of the sun vector. The second pattern happens only for about 4 months of the year and is characterized by the sun spinning around in the x-z plane. This entire analysis of the sun vector was completed on the 103° orbit but apply to the 91° as well.

4.1.2 Optimum Arrangement

Given the sun vector analysis, the solar arrays must capture the most sun on the x-z and x-y planes. The design selected has a hinging panel on either side that will track the sun along with smaller body fixed panels that use the extra space on the satellite. This design makes the smallest impact on the center of mass while generating enough power through both orbits. Both hinging panels move in opposite directions, meaning they have no impact on the center of mass. This design also doesn't have any drag and doesn't affect the propulsion system. These panels can fit into the side of the satellite when they're not in their deployed state.

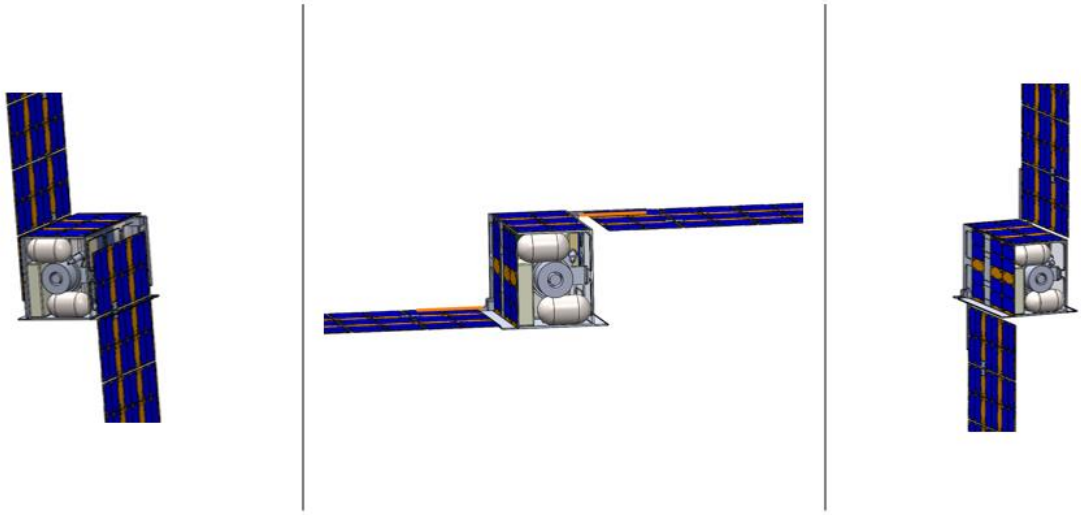

Figure 31: On the left is the POGSat solar array in the 0° configuration. In the middle is POGSat in the 90° configuration. On the right is POGSat in the 180° configuration.

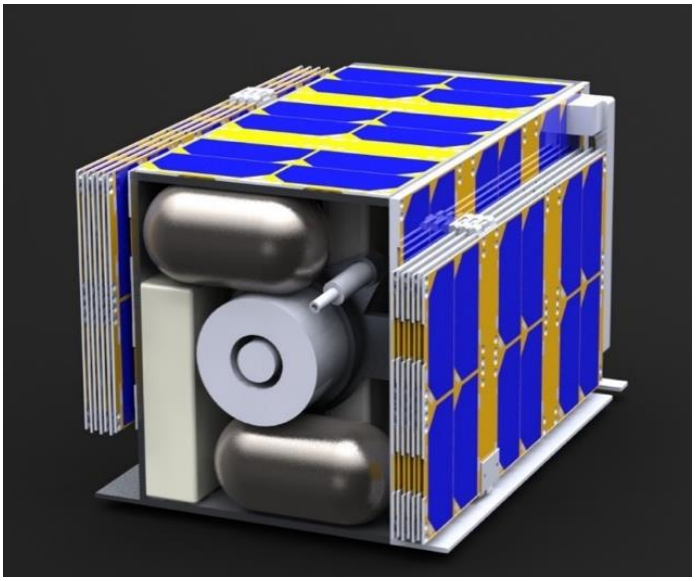

Figure 32: POGSat in the stowed configuration.

4.1.4 STK Modeling

STK has a feature called the Solar panel tool that calculates the power generated using equation (46). Based on the solar panels facing the sun at a given point in time, STK can determine the quantity of pixels under sunlight and at what angle, thus determining the effective area. The structure factor mentioned before is input into the efficiency instead of the A_{eff}.

$$P = \eta W I A_{eff} \tag{43}$$

To use this tool, Blender and COLLADA must be used to generate a dlb file. Using the same dimensions, a Blender model of the POGsat was created. In COLLADA this model was set up to track the sun and different areas were labeled as solar panel groups. The end result from COLLADA is a glb file that can be plugged directly into STK, however the efficiency needs to be accounted for later using Visual Studio Code.

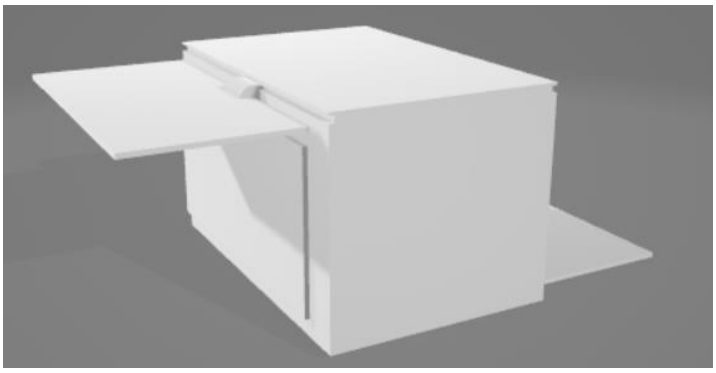

Figure 33: POGSat as a glb file in Microsoft 3D Viewer.

By converting to a gltf file instead of a glb, features of the 3D object can be edited, including the efficiency. Because of the 11% structure factor, the efficiency of these solar panels is 26.255%. In STK itself, the panels can be scaled up or down by factors of 3U, allowing the analysis to use a known quantity of 3U EnduroSat panels. In STK, the panels can also be set to track the sun automatically or be set to a specific angle.

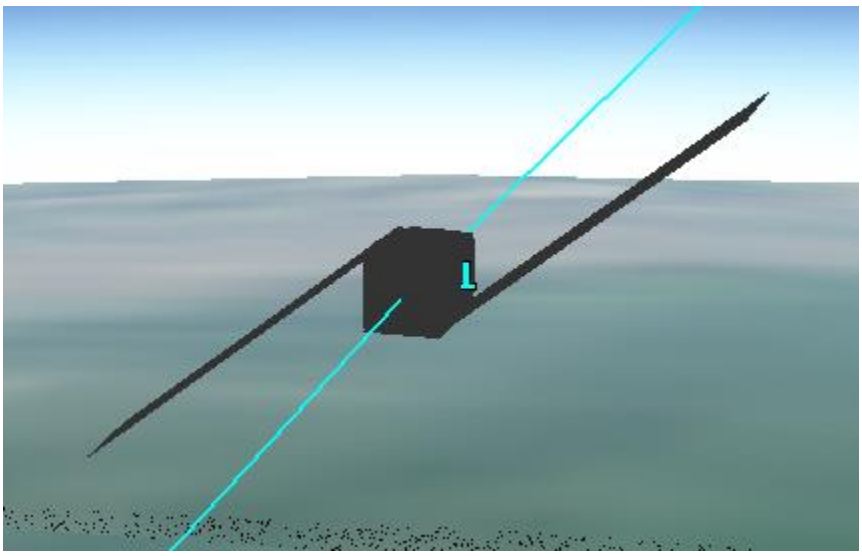

Figure 34: POGSat in a 260km orbit, viewed from STK.

For this project's analysis, the satellite was set to a 260 km orbit in both the 91° and 103° orbits. At this altitude and these inclinations, the satellite is in eclipse for about 35% of its lifetime. Under the "model" section in STK, the model can be uploaded and configured. To start, the arrays were set to a scale factor of 14. These arrays can be seen rotating along with the sun, as intended in the design.

4.1.4 Sizing and Lifetime

To appropriately size the panels, it is necessary to know the desired EOL power and the desired margins for error during spaceflight. Many spacecrafts fly at BOL with double the power they need for EOL. For this satellite, a safety margin of 50W is completely necessary for EOL conditions and the solar panel tool will be used at BOL and EOL to check whether this requirement is being met. At maximum power draw of 105W, that means the panel arrays should generate up to 155W at EOL, or more.

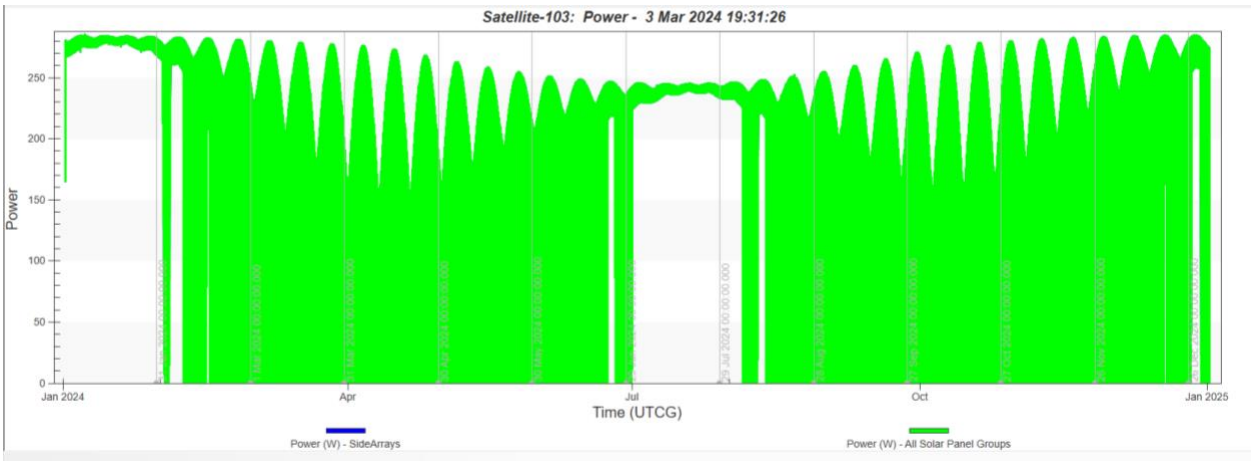

Figure 35: Power generated in 1-hour increments over the course of a year in BOL conditions for 103° orbit.

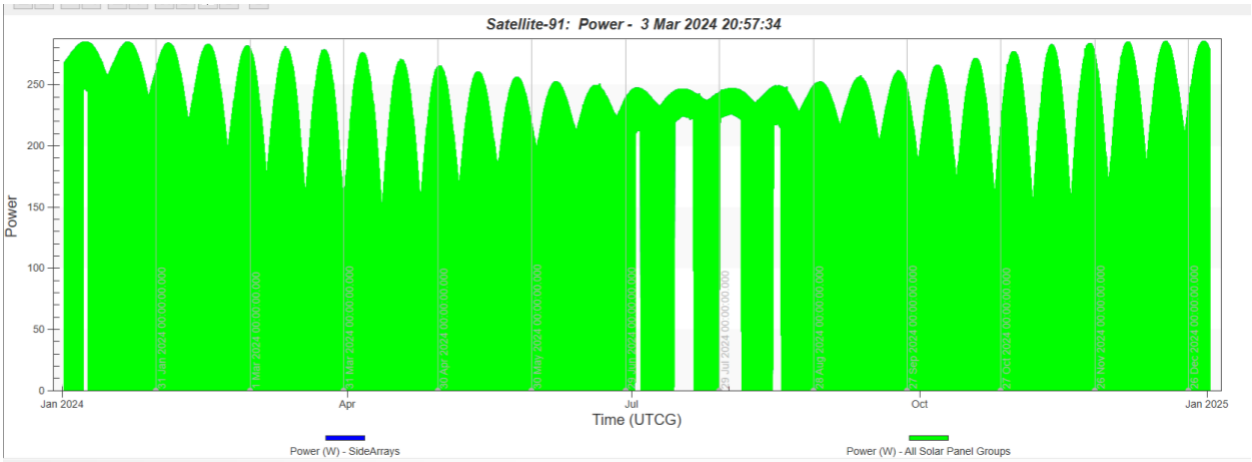

Figure 36: Power generated in 1-hour increments over the course of a year in BOL conditions for 91° orbit.

Each of these plots is the total power generated in 1-hour increments over the course of an entire year. There are times when the power generated can be 0W for a specific measurement, however the more important takeaway is the overall trend in power generation. As can be seen, the trend line for both orbits is well above 155W even at its lowest points. Thus, the array and array size work for both orbits. This analysis was performed on 84U of panels, which equates to 28 3U EnduroSat arrays for the deployed arrays.

The lifetime of solar panels can be modeled using two equations. The EnduroSat panels have a yearly degradation value of 0.017, meaning it loses about 0.017% of its total power generation every year that passes. By multiplying L_d and the efficiency η of the satellite a new efficiency can be plugged into the solar panel tool and tested.

$$L_d = (1 - Y_d)^{current\ life} \tag{44}$$

$$P_{EOL} = P_{BOL} \tag{45}$$

The target mission lifetime for this satellite is 10 years. Doing the math, that makes L_d equal to 0.84 and the new efficiency $\eta = 22.12\%$. At this new efficiency, the power generated is

50W more than is necessary to fly the mission. Given that, over 30U's of cells could break and the mission would still fly to EOL.

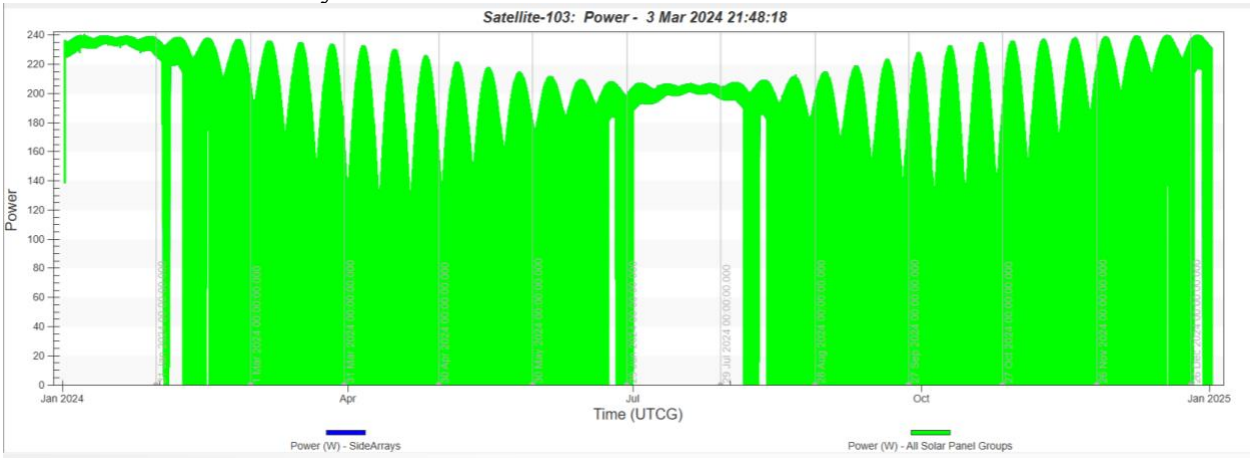

Figure 37: Power generated in 1-hour increments over the course of a year in EOL conditions for 103° orbit.

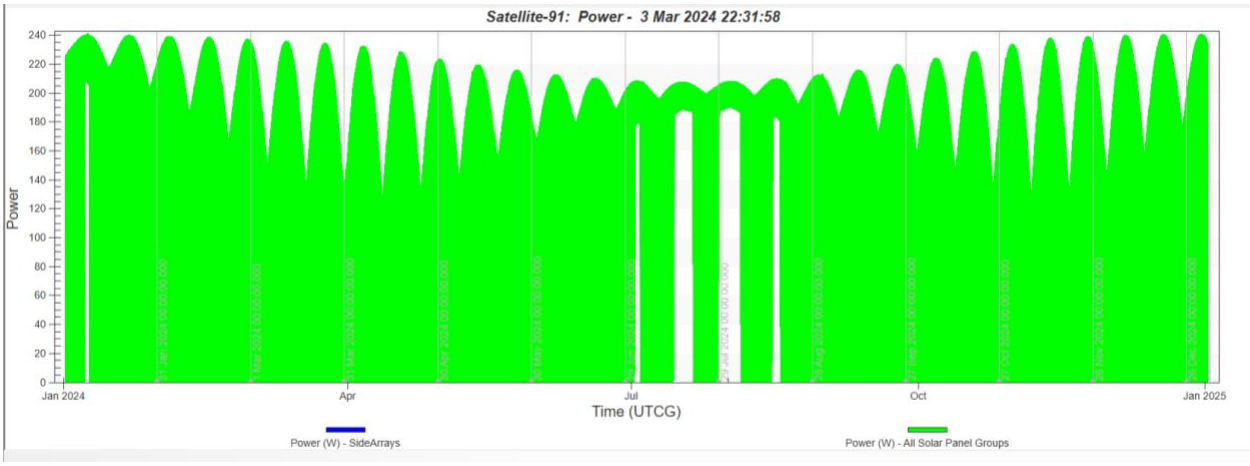

Figure 38: Power generated in 1-hour increments over the course of a year in EOL conditions for 91° orbit.

4.2 Storage and Distribution

The EPS is responsible for delivering power to all parts of the satellite. For this satellite, the propulsion system is by far the most power hungry at 100W. So, the EPS selected must be able to produce over 100W. In addition, the EPS has to fit the physical components of each satellite subsystem and deliver power to smaller, less demanding components. To do this, the EPS will use a direct energy transfer system (DET). This system has been chosen instead of the more traditional maximum power point tracking (MPPT) system. The MPPT is extremely efficient and allows for minimal power losses but is generally more complicated and not well suited to CubeSat applications [70]. Unlike an MPPT system, the DET system makes use of a shunt regulator that sends any extra power from the panels into heat. Power from the storage and generation systems is sent into a power distribution unit with two 5V rails and two 12V rails. These rails are built in parallel to allow for multiple points of failure.

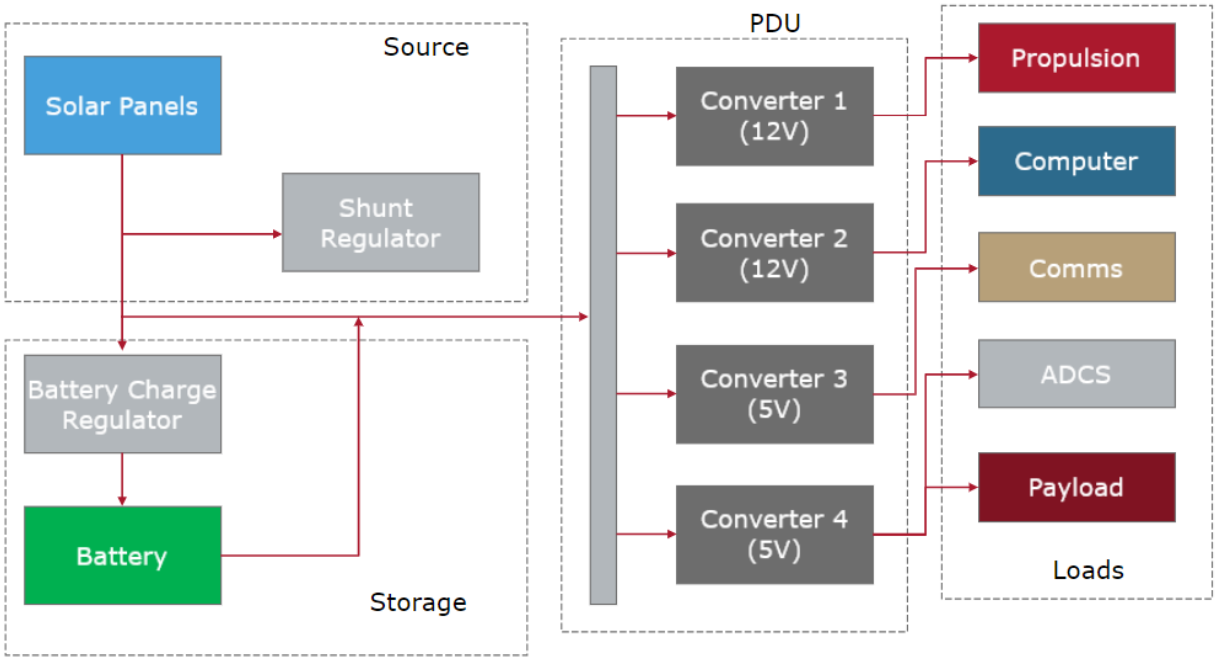

Figure 39: Diagram of the EPS using DET architecture.

4.2.2 Battery

One of the key factors in choosing a battery is its size and depth of discharge (DOD), which can be calculated using equation (46). Due to the low inclinations of both orbits, they experience significant eclipse durations. The maximum power loss during eclipse is estimated to be around 60Whr. Therefore, the battery size should be approximately 300Whr. LiPo batteries are the most suitable option for the CubeSat deployment systems, as they have higher energy density than other battery chemistries. However, LiPo batteries also require temperature regulation to ensure optimal performance.

$$DOD = \frac{P_{OUT}}{P_{TOTAL}} \tag{46}$$

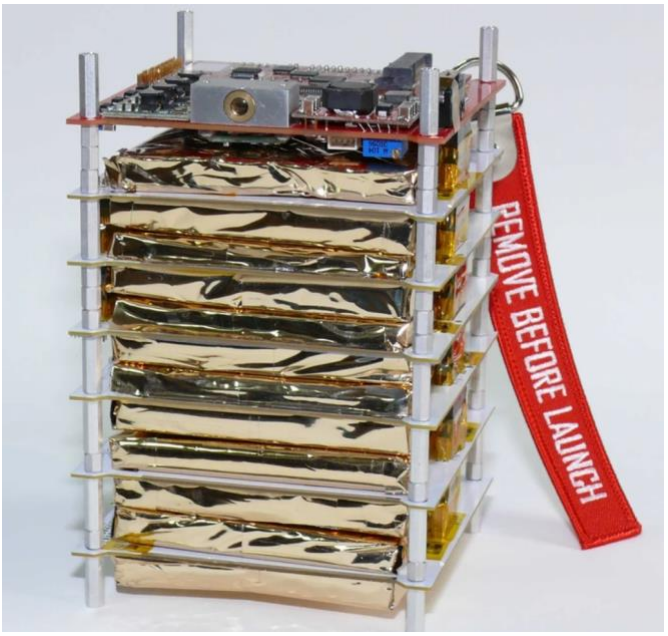

Figure 40: the TITAN-1 battery in preflight state [71].

Given these considerations, the TITAN-1 has been chosen for this satellite [71]. The TITAN-1 is a 350Whr LiPo battery with built in temperature regulation. At 350Whr, it will only lose a maximum 20% of its charge per eclipse and is rated to last up to 10 years with the radiation shielding the satellite currently has. It also supports a maximum charging rate of 300W, which reduces the load on the shunt regulator for charging and increases generation efficiency and distribution.

5 ADC Testbed

The ADC testbed is a system designed by a 2020 MQP to simulate frictionless single axis motion for a satellite. The testbed uses a table and a socket to accomplish this. The table has three reaction wheels that stabilize it and allow it to rotate to a desired attitude. Two of the wheels stabilize the table while the third can rotate freely on the x-y plane (yaw). The socket uses compressed air to create the frictionless environment necessary for experimentation. This system can be controlled remotely using an SSH.

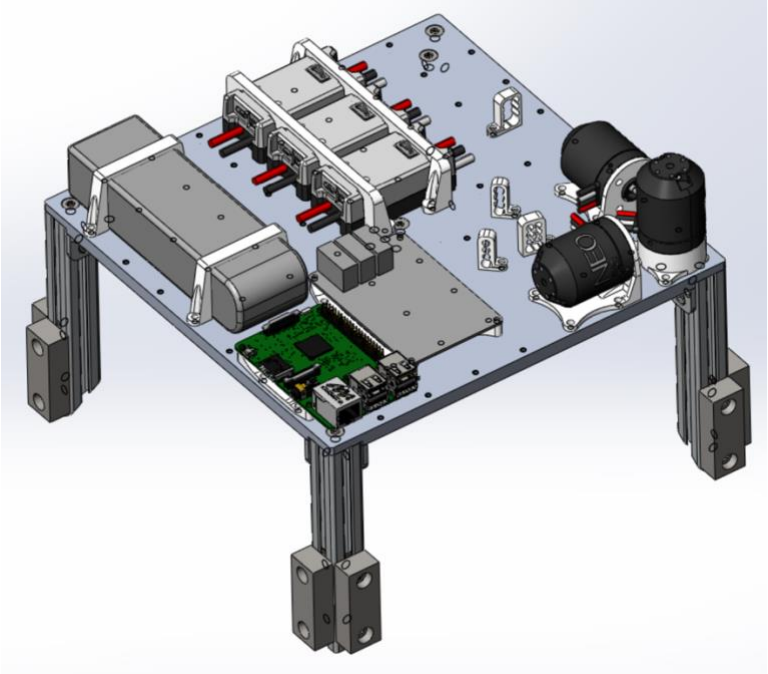

Figure 41: Testbed Flatform from Soildworks [72].

5.1 A-Term Progress

So far, we had been able to connect to the Raspberry Pi and determined that the GUI and Raspberry Pi worked. Unfortunately, when the unit was powered through the control board, the Raspberry Pi functioned improperly. For the reaction wheels to work, the table had to be powered through the control board.

We had determined that the problem was somewhere on the control board or somewhere in the connection from the control board to the Raspberry Pi. Given that, there were a few things that could have been done to fix it. The supply might not have had a high enough current to reach the Raspberry Pi, or the board might have been broken. Either way, the next steps were to look at the electrical diagrams and see why the Pi was not receiving power.

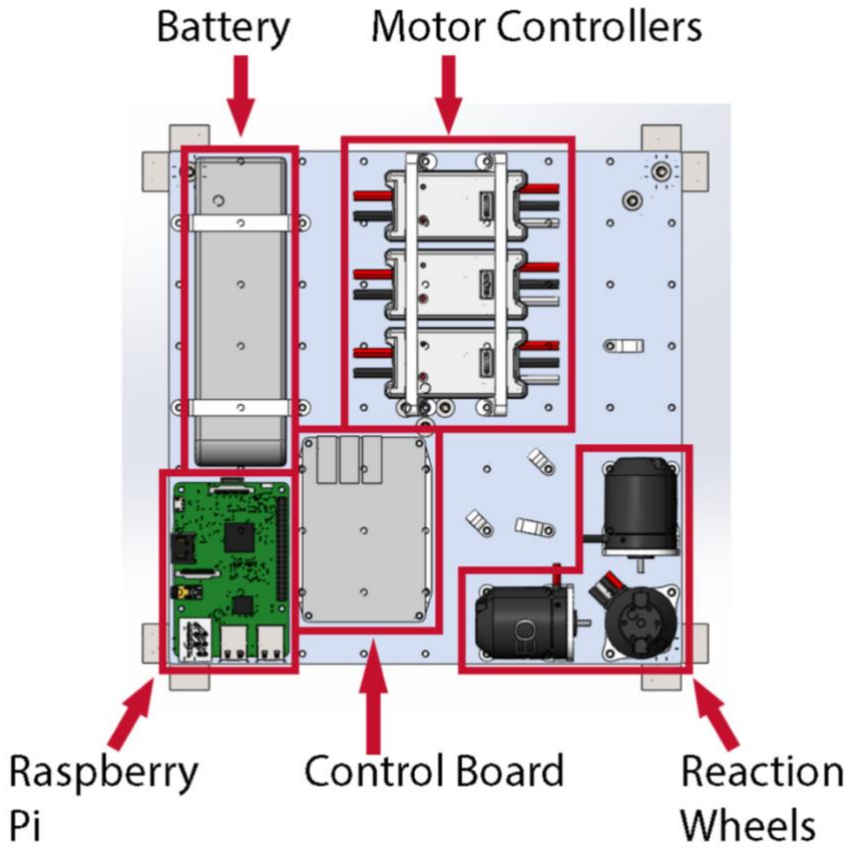

Figure 42: Layout of test flatform [72].

5.2 B-Term Progress

We have completely reworked the CubeSat Control board, which included soldering joints and replacing components to help get the board back to a working state. Additionally, fixing all power issues were done with modifying the charger to ensure that the battery would charge alongside a backup battery for the entire system was procured and test in which it worked.

For the future, the overheating of the control board needs to be fixed. This is a critical failure and was directly impacting the amount of power that the motor drivers should handle and how well they can control each of the reaction wheels. The other item of note that needs to be addressed is when the system is on and active the reaction wheels are rather weak and sound like they are at their minimum power requirements.

5.3 C-Term Progress

The testbed issues have been fixed, the new battery system works, and the old system also now works again. Documentation has been created in the lab regarding the process of charging the testbed. After everything was gone through again, the entire system was working as expected with no issues. The reaction wheels are reorienting the test stand as expected and with reasonable slew rates.

5.4 Future Changes and Improvements

The work on the test stand is not complete as there are several features that could be implemented in the future. As the test stand is based on reaction wheels as a method of reorientation it could be changed to a magnetorquer system using the Helmholtz Cage. The entire code for the Raspberry Pi could be modified to create a pointing system instead of the current level program which the test stand tries to level itself regardless of the orientation. This modified pointing system could have a laser pointer and hit a goal some distance away to test accuracy of the system.

6 Conclusions

In conclusion, the development of the Polar-Orbiting Gravimetry CubeSat (POGSat) marks an advancement in our ability to measure and understand the Earth's gravitational field with high precision and cost-effectiveness. Through the innovative design of a 12U CubeSat, this research has successfully demonstrated a scalable and efficient approach to global gravimetry that surpasses the capabilities of previous missions such as the Gravity Field and Steady-State Ocean Circulation Explorer (GOCE). The strategic use of dual satellites in high-inclination orbits ensures comprehensive coverage of the Earth's surface, including previously underrepresented polar regions, thereby enhancing the quality and completeness of gravitational data.

The successful development and implementation of a high-precision gradiometer, alongside robust systems for attitude determination, control, propulsion, power generation, and communications, underscore the CubeSat's potential to contribute significantly to our understanding of geophysical processes and climate change. The application of advanced simulation tools such as Systems Tool Kit (STK®) for orbital and environmental analysis, alongside SolidWorks and Ansys for mechanical design and analysis, has been instrumental in optimizing the CubeSat's design for its mission objectives.

The POGSat project's integration of cutting-edge technology and methodologies in CubeSat design not only paves the way for future gravitational field missions but also serves as a blueprint for leveraging small satellite platforms in addressing complex scientific challenges. This mission underscores the potential of CubeSats to play a pivotal role in the next generation of Earth observation and space research, offering a viable path toward achieving high-impact scientific goals within the constraints of budget and resources. As we look to the future, the lessons learned, and successes achieved through the POGSat mission will undoubtedly inspire and inform the development of new technologies and approaches in satellite engineering and Earth sciences.

6.1 Subteam Outcomes

ADCS (Attitude Determination and Control System)

The ADCS team has focused on developing a Continuous Discrete Extended Kalman Filter (CD-EKF) for accurate attitude determination, crucial for maintaining the CubeSat's orientation in orbit. This development began in MATLAB, with plans to transition the code to Python or C for the flight computer. Simulink is being used to facilitate the creation of the EKF. The team has chosen a magnetorquer as the actuator, considering its suitability for the mission's requirements.

GNC (Guidance, Navigation, and Control)

The GNC team's efforts have concentrated on selecting high-precision sensors and developing an in-house GPS system for enhanced navigation accuracy. Additionally, they are implementing a telemetry system using an Iridium 9602 satellite modem combined with a UHF/VHF system for reliable data transmission. Work is also progressing on a system model and on-board computer to ensure efficient mission operations.

Power

The Power team has managed the CubeSat's energy needs by optimizing solar panel placement, avoiding the need for deployment mechanisms and reducing drag. This approach simplifies ADCS operations and ensures energy efficiency. The team remains prepared to explore deployment options if the power requirements increase, demonstrating a balanced approach to mission design and flexibility.

References & Bibliography

1. GOCE - Earth Online [Internet]. earth.esa.int. Available from: https://earth.esa.int/eogateway/missions/goce
2. EGG Overview - Earth Online [Internet]. earth.esa.int. Available from: https://earth.esa.int/eogateway/instruments/egg/description
3. GOCE Mission Requirements Document Noordwijk The Netherlands [Internet]. 2000 [cited 2023 Oct 3]. Available from: https://esamultimedia.esa.int/docs/GO-RS-ESA-SY-0001.PDF
4. Satellite Gravimetry [Internet]. GGOS. Available from: https://ggos.org/item/satellite-gravimetry/
5. Rummel, R. (2010). GOCE: Gravitational Gradiometry in a Satellite. In: Freeden, W., Nashed, M.Z., Sonar, T. (eds) Handbook of Geomathematics. Springer, Berlin, Heidelberg. https://doi.org/10.1007/978-3-642-01546-5_4
6. Johannessen, J. A., Balmino, G., Le Provost, C., Rummel, R., Sabadini, R., Sünkel, H., Tscherning, C. C., Visser, P., Woodworth, P., Hughes, C., Legrand, P., Sneeuw, N., Perosanz, F., Aguirre-Martinez, M., Rebhan, H., & Drinkwater, M. (2003). The European Gravity Field and Steady-State Ocean Circulation Explorer Satellite Mission Its Impact on Geophysics. *Surveys in Geophysics*, *24*(4), 339–386. https://doi.org/10.1023/B:GEOP.0000004264.04667.5e
7. Spherical Harmonic Representation of the Gravity Field Potential 1 Introduction [Internet]. [cited 2023 Oct 3]. Available from: https://spsweb.fltops.jpl.nasa.gov/portaldataops/mpg/MPG_Docs/Source%20Docs/gravity-SphericalHarmonics.pdf
8. Space debris: Feel the burn. ESA. (2021, April 28). Retrieved October 5, 2023, from:https://www.esa.int/Space_Safety/Clean_Space/Space_debris_feel_the_burn#.Y_j2QJRRAL8.link
9. Flechtner, F., Reigber, C., Rummel, R. *et al.* Satellite Gravimetry: A Review of Its Realization. *Surv Geophys* **42**, 1029–1074 (2021). https://doi.org/10.1007/s10712-021-09658-0
10. GRACE - Earth Online [Internet]. earth.esa.int. Available from: https://grace.jpl.nasa.gov/mission/grace/
11. GRACE Instruments - Earth Online [Internet]. earth.esa.int. Available from: https://earth.esa.int/eogateway/missions/grace#instruments-section
12. Frommknecht, Björn & H, Oberndorfer & Flechtner, F. & R, Schmidt. (2003). Integrated sensor analysis for GRACE - Development and validation. Advances in Geosciences. 1. 10.5194/adgeo-1-57-2003.
13. B. D. Tapley, S. Bettadpur, M. M. Watkins and Ch. Reigber, The Gravity Recovery and Climate Experiment: Mission Overview and Early Results, Geophys. Res. Lett., 31, L09607, doi:10.1029/2004GL019920, 2004.
14. Massotti, L., Bulit, A., Daras, I., Carnicero Dominguez, B., Carraz, O., Hall, K., Heliere, A., March, G., Marchese, V., Martimort, P., Palmer, K., Rodrigues, G., Silvestrin, P., and Wallace, N.: Next Generation Gravity Mission design activities within the MAGIC - MAss Change and Geoscience International - Constellation, EGU General Assembly 2023, Vienna, Austria, 24–28 Apr 2023, EGU23-14482, https://doi.org/10.5194/egusphere-egu23-14482, 2023.

15. Craig, C. CubeSats for Environmental Monitoring (Conference Presentation), Proc. SPIE 11530, Sensors, Systems, and Next-Generation Satellites XXIV, 1153002 (23 September 2020); https://doi.org/10.1117/12.2582821
16. Belvin, W, et al. *ADVANCED DEPLOYABLE STRUCTURAL SYSTEMS for SMALL SATELLITES*. 2016.
17. University, Utah State. "GASPACS CubeSat | Projects | GAS | Physics." *www.usu.edu*, www.usu.edu/physics/gas/projects/gaspacs.
18. Reveles, J, et al. *SSC17-II-08 In-Orbit Performance of AstroTube™: AlSat Nano's Low Mass Deployable Composite Boom Payload*.
19. *What Are SmallSats and CubeSats? - NASA*. www.nasa.gov/what-are-smallsats-and-cubesats/.
20. The Sun sets on the Arctic melt season - National Snow and Ice Data Center [Internet]. nsidc.org. Available from: https://nsidc.org/arcticseaicenews/2023/10/the-sun-sets-on-the-arctic-melt-season/
21. *BGT-X5 monoprop*. Busek (n.d.). Retrieved October 10, 2023, from https://static1.squarespace.com/static/60df2bfb6db9752ed1d79d44/t/61292af2a097083a87c4cbc0/1630087925107/BGT_X5_v1.0.pdf
22. *MPS-130 Innovative Propulsion Solutions for SmallSats*. Aerojet Rocketdyne (n.d.). Retrieved October 10, 2023, from https://www.rocket.com/sites/default/files/documents/CubeSat/MPS-130%20data%20sheet%20crop.pdf
23. *Comet: Water-based Propulsion for Small Satellites*. Bradford Space (n.d.). Retrieved October 10, 2023, from https://satcatalog.s3.amazonaws.com/components/897/SatCatalog_-_Bradford_Space_-_Comet-1000_-_Datasheet.pdf?lastmod=20210710014123
24. *MONOPROPELLANT PROPULSION UNIT FOR CUBESATS (MPUC) SYSTEM LOW FLAME TEMPERATURE GREEN MONOPROPELLANT*. Champaign Urbana Aerospace, July 2020. Retrieved October 10, 2023, from https://satcatalog.s3.amazonaws.com/components/910/SatCatalog_-_Champaign-Urbana_Aerospace_-_MPUC_1.5U_-_Datasheet.pdf?lastmod=20210806035351
25. *CubeDrive Brochure*. Dawn Aerospace (n.d.). Retrieved October 10, 2023, from https://static1.squarespace.com/static/5e82736a5e6bb91e8af13ea7/t/6407332000c0a0548186d9f4/1678193441552/DA14+CubeDrive+Brochure+20230301.pdf
26. *MONOPROPELLANT PROPULSION MODULE*. Moog (n.d.). Retrieved October 10, 2023, from https://www.moog.com/content/dam/moog/literature/sdg/space/propulsion/moog-monopropellant-propulsion-module-datasheet.pdf
27. *SmallSat Propulsion System EPSS*. Nano Avionics (n.d.). Retrieved October 10, 2023, from https://nanoavionics.com/cubesat-components/cubesat-propulsion-system-epss/
28. *A4 CubeDrive Brochure*. Dawn Aerospace (n.d.). Retrieved October 10, 2023, from https://satcatalog.s3.amazonaws.com/components/1001/SatCatalog_-_Dawn_Aerospace_-_0.8U_CubeDrive_-_Datasheet.pdf?lastmod=20220429194829
29. *JPL MarCO - Micro CubeSat Propulsion System*. VACCO (n.d.). Retrieved October 10, 2023, from https://www.vacco.com/images/uploads/pdfs/JPL_MarCO_-_Micro_CubeSat_Propulsion_System_datasheet.pdf

30. *DFAST CubeSat Warm gas Thruster*. Benchmark Space Systems (n.d.). Retrieved October 10, 2023, https://satcatalog.s3.amazonaws.com/components/1083/SatCatalog_-_Benchmark_Space_Systems_-_Starling_0.5U_-_Datasheet.pdf?lastmod=20210717002219
31. *MiPS Standard*. VACCO (n.d.). Retrieved October 10, 2023, from https://www.vacco.com/images/uploads/pdfs/MiPS_standard_0714.pdf
32. *MEPSI Micro Propulsion System*. VACCO (n.d.). Retrieved October 10, 2023, from https://cubesat-propulsion.com/wp-content/uploads/2015/10/Mepsi-micro-propulsion-system.pdf
33. *NanoProp 6DOF*. GomSpace (n.d.). Retrieved October 10, 2023, from https://gomspace.com/UserFiles/Subsystems/flyer/Flyer_NanoProp_6DOF.pdf
34. *NanoProp 20000*. GomSpace (n.d.). Retrieved October 10, 2023, from https://gomspace.com/UserFiles/Subsystems/flyer/Flyer_NanoProp_20000.pdf
35. *Reaction Control Propulsion Module*. VACCO (n.d.). Retrieved October 10, 2023, from https://cubesat-propulsion.com/wp-content/uploads/2022/04/X13003000-01_RCM_2016update.pdf
36. *CuSP Propulsion System*. VACCO (n.d.). Retrieved October 10, 2023, from https://cubesat-propulsion.com/wp-content/uploads/2017/08/X16038000-01-data-sheet-080217.pdf
37. *nanoFEEP*. Morpheus Space (n.d.). Retrieved October 10, 2023, from https://satcatalog.s3.amazonaws.com/components/981/SatCatalog_-_Morpheus_Space_-_nanoFEEP_-_Datasheet.pdf?lastmod=20210710023905
38. *BET-MAX v1.0*. Busek (n.d.). Retrieved October 10, 2023, from https://static1.squarespace.com/static/60df2bfb6db9752ed1d79d44/t/61292b0fa097083a87c4ce1f/1630087953271/BETMAX_v1.0.pdf
39. Krejci, D., Mier-Hicks, F., Fucetola, C., Lozano, P., Hsu Schouten, A., and Martel, F. "Design and Characterization of a Scalable ion Electrospray Propulsion System," ISTS Paper b-149, July 2010. https://electricrocket.org/IEPC/IEPC-2015-149_ISTS-2015-b-149.pdf
40. Kristina Lemmer, Propulsion for CubeSats, Acta Astronautica, Volume 134, 2017, pp. 231-243, ISSN 0094-5765, https://doi.org/10.1016/j.actaastro.2017.01.048.
41. *BHT-100 v1.0*. Busek (n.d.). Retrieved October 10, 2023, from https://static1.squarespace.com/static/60df2bfb6db9752ed1d79d44/t/6154811d7ac4036af765f736/1632928031263/BHT_100_v1.0.pdf
42. *ThrustMe*. ThrustMe (n.d.). Retrieved October 10, 2023, from https://www.thrustme.fr/base/stock/ProductBannerFiles/2_thrustme-npt30-i2.pdf
43. *MPS-120 Innovative Propulsion Solutions for SmallSats*. Aerojet Rocketdyne (n.d.). Retrieved October 10, 2023, from https://www.rocket.com/sites/default/files/documents/CubeSat/MPS-120%20data%20sheet-single%20sheet.pdf
44. *BIT3 v1.0*. Busek (n.d.). Retrieved October 10, 2023, from https://static1.squarespace.com/static/60df2bfb6db9752ed1d79d44/t/610c4176ad8cb2543959e7a6/1628193142983/BIT3_v1.0.pdf
45. Gurciullo, A., Jarrige, J., Lascombes, P., and Packan, D. "Experimental performance and plume characterisation of a miniaturised 50W Hall thruster". In 36th International Electric Propulsion Conference, Vienna, Austria, 2019.

46. *TILE 2*. Accion Systems (n.d.). Retrieved October 10, 2023, from https://satcatalog.s3.amazonaws.com/components/965/SatCatalog_-_Accion_Systems_-_TILE_2_-_Datasheet.pdf?lastmod=20210710023124
47. *TILE 3*. Accion Systems (n.d.). Retrieved October 10, 2023, from https://satcatalog.s3.amazonaws.com/components/1299/SatCatalog_-_Accion_Systems_-_TILE_3_-_Datasheet.pdf?lastmod=20220216045341
48. Nie Y, Shen Y, Chen Q. Combination Analysis of Future Polar-Type Gravity Mission and GRACE Follow-On. *Remote Sensing*. 2019; 11(2):200. https://doi.org/10.3390/rs11020200
49. Purkhauser AF, Pail R. Triple-Pair Constellation Configurations for Temporal Gravity Field Retrieval. *Remote Sensing*. 2020; 12(5):831. https://doi.org/10.3390/rs12050831
50. Sutton, G. P., & Biblarz, O. (2017). Rocket Propulsion Elements. John Wiley & Sons, Inc.
51. M. Yu. Ovchinnikov, D. S. Roldugin, V. I. Penkov: Three-Axis Active Magnetic Attitude Control Asymptotical Study. In: Acta Astronautica 110, 2015, p. 279-286.
52. Tapley, B.D., Watkins, M.M., Flechtner, F. et al. Contributions of GRACE to understanding climate change. Nat. Clim. Chang. 9, 358–369 (2019). https://doi.org/10.1038/s41558-019-0456-2
53. Kamboj, A. et al. (2023). Solar Panel Deployment Mechanism for Nano-Satellite. In: Prakash, C., Rao, V.S., Murthy, D.V.A.R. (eds) Smart Small Satellites: Design, Modelling and Development. Lecture Notes in Electrical Engineering, vol 963. Springer, Singapore. https://doi.org/10.1007/978-981-19-7198-3_12
54. Wilfried Ley/Klaus Wittmann/Willi Hallmann, Handbook of Space Technology, John Wiley and Sons, Ltd. 2009
55. F. Landis Markley, John L. Crassidis, Fundamentals of Spacecraft Attitude Determination and Control. Space Technology Library.
56. NEO-6 GPS Modules Datasheet. u-blox. [cited 2023 Dec 16]. Available from: https://www.digikey.com/en/datasheets/sparkfun-electronics/sparkfun-electronics-neo-6-datasheet
57. ADF7023-J: High Performance, Low Power, ISM Band FSK/GFSK/MSK/GMSK Transceiver IC Data Sheet. Analog Devices. [cited 2023 Dec 16]. Available from: http://www.analog.com
58. Iridium 9602 Module Datasheet. Iridium Satellite Communications. [cited 2023 Dec 16]. Available from: https://www.iridium.com/products/iridium-9602/
59. UHF Transceiver II CubeSat Communication. EnduroSat. [cited 2023 Dec 16]. Available from: https://www.endurosat.com/cubesat-store/cubesat-communication-modules/uhf-transceiver-ii/
60. IMTQ Magnetoruqer Board Datasheet, ISISPACE. ISIS - Innovative Solutions In Space. [cited 2023 Dec 16]. Available from: https://www.isispace.nl/downloads/
61. Gen 2 CubeTorquer CR0006. CubeSatShop. [cited 2023 Dec 16]. Available from: https://www.cubesatshop.com/product/gen-2-cubetorquer-cr0006/
62. Gen 2 CubeADCS Core. CubeSatShop. [cited 2023 Dec 16]. Available from: https://www.cubesatshop.com/product/gen-2-cubeadcs-core/
63. International Geomagnetic Reference Field. National Oceanic and Atmospheric Administration (NOAA). [cited 2023 Dec 16]. Available from: https://www.ngdc.noaa.gov/IAGA/vmod/igrf.html

64. GNSS Patch Antenna. ISIS Space. (ISIS). [cited 2024 Jan 28]. Available from: https://www.isispace.nl/product/gnss-patch-antenna/
65. EXA GCA01. Ecuadorian Space Agency (EXA). [cited 2024 Feb 2]. Available from: https://satsearch.co/products/exa-gca01-compact-gnss-active-patch-antenna
66. ISIS CubeSat 1U-3U UHF/VHF Antenna System. ISIS Space. (ISIS). [cited 2024 Feb 3]. Available from: https://www.isispace.nl/product/cubesat-antenna-system-1u-3u/
67. "An overview of sun sensors available on the global marketplace for space," Satsearch blog, Feb. 12, 2020. https://blog.satsearch.co/2020-02-12-sun-sensors-an-overview-of-systems-available-on-the-global-marketplace-for-space
68. https://endurosat.com/cubesat-store/cubesat-solar-panels/3u-solar-panel-xy/
69. 3U Solar Panel CubeSat Solar Panel. (n.d.). CubeSat by EnduroSat. https://endurosat.com/cubesat-store/cubesat-solar-panels/3u-solar-panel-xy/
70. Gujarathi, D., Smith, K., & Workinger, B. (2023). CubeSat Development for Identification of Space Debris. : Worcester Polytechnic Institute.
71. TITAN-1: 350Whr Cubesat Compact Battery Pack| CubeSat.Market. (n.d.). Cubesat Market. Retrieved March 3, 2024, from https://www.cubesat.market/titan1-battery-matrix
72. Galliath, Robaire, et al. "Design and Analysis of a CubeSat." *Major Qualifying Project*, Worcester Polytechnic Institute, 2020.

Appendix A: Beta ADCS Detumble Phase Software

Below is an early version of the ADCS Detumble phase code for the satellite. Please note that the code is in Python. It is rather oversimplified, but it implements all basic aspects needed of the ADCS system mode 1.

```
import numpy as np
import matplotlib.pyplot as plt

class ExtendedKalmanFilter3AxisDynamic:
    def __init__(self, inertia):
        self.x = np.zeros(6)
        self.P = np.eye(6)
        self.F_jacobian = np.eye(6)
        for i in range(3):
            self.F_jacobian[i, i+3] = 1
        self.H_jacobian = np.zeros((12, 6))
        self.H_jacobian[0:3, 3:6] = np.eye(3)
        self.R = np.eye(12) * 0.01
        self.Q = np.eye(6) * 0.01
        self.inertia = np.array(inertia)

#Prediction Step
    def predict(self, torques):
        angular_accel = torques / self.inertia[3:6]
        self.x[3:6] += angular_accel
        self.x[0:3] += self.x[3:6]
        self.P = self.F_jacobian @ self.P @ self.F_jacobian.T + self.Q

#Update Step
    def update(self, z):
        K = self.P @ self.H_jacobian.T @ np.linalg.inv(self.H_jacobian @ self.P @
self.H_jacobian.T + self.R)
        h = self.H_jacobian @ self.x
        self.x += K @ (z - h)
        self.P = (np.eye(6) - K @ self.H_jacobian) @ self.P
#Recursive get state function
    def get_state(self):
        return self.x


#PID controller for the Control System

def measure_magnetic_field(t):
    """Simulate a rotating magnetic field in the X-Z plane."""
    B0 = 2e-5
```

```
    omega = 2 * np.pi / 600  # Simulating a 10-minute orbital period
    Bx = B0 * np.cos(omega * t)
    Bz = B0 * np.sin(omega * t)
    return np.array([Bx, 0, Bz])

def b_dot_control_law(B, B_prev, k):
    delta_B = B - B_prev
    m = -k * delta_B
    return m

def check_detumbled_condition(angular_velocity, threshold=0.01):
    return np.all(np.abs(angular_velocity) < threshold)

# Constants
k = 1e4  # Selected gain for B-dot control
max_torque = 0.01  # Maximum allowable torque per axis in Nm
dt = 0.1  # Time step
num_steps = 500

# Initialization
ekf = ExtendedKalmanFilter3AxisDynamic(inertia=[0.05, 0.05, 0.05, 0.05, 0.05, 0.05])
initial_rot_rad_s = np.array([0.1, 1, 10]) * (2 * np.pi / 60)
ekf.x = np.array([10.0, 10.0, 10.0, *initial_rot_rad_s])

# Execute the B-dot control detumble loop with the time-varying magnetic field
B_prev = measure_magnetic_field(0)
torques = []
orientations = []
angular_velocities = []

for t in np.arange(0, num_steps*dt, dt):
    B = measure_magnetic_field(t)
    m = b_dot_control_law(B, B_prev, k)
    torque = np.clip(m, -max_torque, max_torque)
    torques.append(torque)
    ekf.predict(torque)
    orientations.append(ekf.x[:3])
    angular_velocities.append(ekf.x[3:6])
    B_prev = B
    if check_detumbled_condition(ekf.x[3:6]):
        break

torques = np.array(torques)
orientations = np.array(orientations)
angular_velocities = np.array(angular_velocities)
```

```
# Visualizations

import matplotlib.pyplot as plt

# Visualizing angular velocities, orientations, and applied torques
fig, axes = plt.subplots(3, 1, figsize=(10, 12), sharex=True)

# Orientation
axes[0].plot(orientations)
axes[0].set_ylabel('Orientation (rad)')
axes[0].legend(['Roll', 'Pitch', 'Yaw'])
axes[0].set_title('Orientation During Detumbling (B-dot Control)')

# Angular Velocities
axes[1].plot(angular_velocities)
axes[1].set_ylabel('Angular Velocity (rad/s)')
axes[1].legend(['Roll', 'Pitch', 'Yaw'])
axes[1].set_title('Angular Velocity During Detumbling (B-dot Control)')

# Applied Torques
axes[2].plot(torques)
axes[2].set_ylabel('Torque (Nm)')
axes[2].set_xlabel('Time (s)')
axes[2].legend(['X', 'Y', 'Z'])
axes[2].set_title('Applied Torques During Detumbling (B-dot Control)')

plt.tight_layout()
plt.show()
```

Appendix B: Beta ADCS Science Phase Software

Below is the beta code for the ADCS system when running mode 2 which is the science mode. This code is rather simple; however, it works.

```
#Combined ADCS system for 12U CubeSat Ver. 0.22
#10/09/2023

#Includes:
   #Interia
   #Intial Conditions
   #Gausian white noise
   #Max Tourque
   #PID Controller for the Magnetourqer actuator
   #EFK (Extended Kalman Filter) for attitude determination
   #Jacobian


#Assumptions:
   #Interia=0.05kgm^2 (per axis)
   #Max Magnetourquer Tourque=0.05Nm
   #Steady contitions


#Notes
#100 Time Steps
#dt=0.1

#Needs to be done:
   #Improve PID controller as right now it does basically nothing
   #Add certientity


import numpy as np
import matplotlib.pyplot as plt

#EKF Class
class ExtendedKalmanFilter3AxisDynamic:
   def __init__(self, inertia):
      self.x = np.zeros(6)
      self.P = np.eye(6)
      self.F_jacobian = np.eye(6)
      for i in range(3):
         self.F_jacobian[i, i+3] = 1
      self.H_jacobian = np.zeros((12, 6))
      self.H_jacobian[0:3, 3:6] = np.eye(3)
```

```
        self.R = np.eye(12) * 0.01
        self.Q = np.eye(6) * 0.01
        self.inertia = np.array(inertia)

#Prediction Step
    def predict(self, torques):
        angular_accel = torques / self.inertia[3:6]
        self.x[3:6] += angular_accel
        self.x[0:3] += self.x[3:6]
        self.P = self.F_jacobian @ self.P @ self.F_jacobian.T + self.Q

#Update Step
    def update(self, z):
        K = self.P @ self.H_jacobian.T @ np.linalg.inv(self.H_jacobian @ self.P @
self.H_jacobian.T + self.R)
        h = self.H_jacobian @ self.x
        self.x += K @ (z - h)
        self.P = (np.eye(6) - K @ self.H_jacobian) @ self.P
#Recursive get state function
    def get_state(self):
        return self.x


#PID controller for the Control System
class PIDController3AxisLimited:
    def __init__(self, Kp, Ki, Kd, max_torque):
        self.Kp = Kp
        self.Ki = Ki
        self.Kd = Kd
        self.max_torque = max_torque
        self.prev_error = np.zeros(3)
        self.integral = np.zeros(3)

#Calculation of PID
    def compute(self, setpoint, actual_position, dt):
        error = setpoint - actual_position
        self.integral += error * dt
        derivative = (error - self.prev_error) / dt
        output = self.Kp * error + self.Ki * self.integral + self.Kd * derivative
        output = np.clip(output, -self.max_torque, self.max_torque)
        self.prev_error = error
        return output


#Definintions of EKF & PID
ekf = ExtendedKalmanFilter3AxisDynamic(inertia=[0.05, 0.05, 0.05, 0.05, 0.05, 0.05])
```

```
#Default: Kp=0.1,Ki=0.01,Kd=0.01
pid = PIDController3AxisLimited(0.1, 0.02, 0.005, max_torque=0.05)


#Initial Conditions Setup
use_custom_initial_conditions = True
if use_custom_initial_conditions:
    ekf.x = np.array([10.0, 10.0, 10.0, 0.1, 0.1, 0.1])

#Wanted final output degrees
setpoint = np.array([45.0, 45.0, 45.0])
dt = 0.1
num_steps = 100
torques = []
orientations = []
#Input Sensor Data
gyroscope_data = np.array([0.0, 0.0, 0.0])
magnetometer_data = np.array([0.0, 0.0, 0.0])
sun_sensors_data = np.array([0.0, 0.0, 0.0, 0.0, 0.0, 0.0])

#Recusive loops for EFK & PID
for _ in range(num_steps):
    noisy_gyroscope_data = gyroscope_data + np.random.normal(0, 0.01, size=3)
    noisy_magnetometer_data = magnetometer_data + np.random.normal(0, 0.01, size=3)
    noisy_sun_sensors_data = sun_sensors_data + np.random.normal(0, 0.01, size=6)
    measurements = np.concatenate([noisy_gyroscope_data, noisy_magnetometer_data,
noisy_sun_sensors_data])
    estimated_orientation = ekf.get_state()[0:3]
    control_output = pid.compute(setpoint, estimated_orientation, dt)
    ekf.predict(control_output)
    ekf.update(measurements)
    torques.append(control_output)
    orientations.append(estimated_orientation)

torques = np.array(torques)
orientations = np.array(orientations)

#Ploting
fig, axes = plt.subplots(2, 3, figsize=(15, 10))
axes_list = ['X', 'Y', 'Z']
for i, axis in enumerate(axes_list):
    axes[0, i].plot(torques[:, i])
    axes[0, i].set_title(f"Torque in {axis} Axis")
    axes[0, i].set_xlabel("Time Steps")
    axes[0, i].set_ylabel("Torque")
    axes[0, i].grid(True)
```

```
    axes[1, i].plot(orientations[:, i])
    axes[1, i].set_title(f"Orientation in {axis} Axis")
    axes[1, i].set_xlabel("Time Steps")
    axes[1, i].set_ylabel("Orientation")
    axes[1, i].grid(True)

plt.tight_layout()
plt.show()
```

Appendix C

Microstrip Fed Patch Antenna

A Microstrip Fed Patch Antenna is a type of antenna that is used for many different applications on and off the Earth. Its design is not that different to a normal patch antenna. The main benefits of a patch antenna are that they are rather low profile and do not require much space. The reason that a non-COTs option would be considered as the need for an extremely high accuracy GPS system then it starts with the receiving of the GPS signals which requires an antenna.

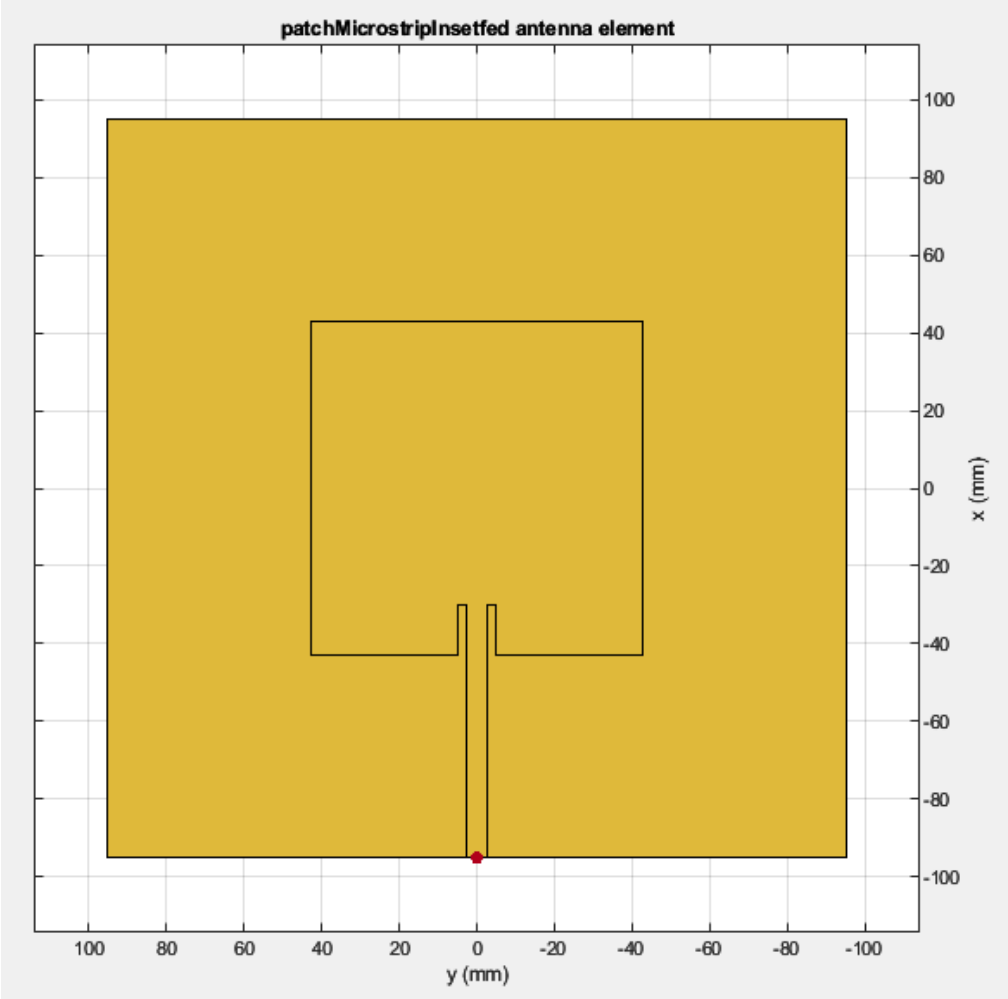

Figure 43 : Microstrip infed antenna design using MATLAB Antenna Designer

The design also includes the directionality of the antenna. Which is a classification of antennas in which the gain (or rather how strong the signal is) in one particular direction. This may seem like a negative thing to have your antenna only be good in one direction but that is helpful as our CubeSat will be always oriented towards the GPS constellation. However, with that being said, the antenna will be able to receive a GPS signal in every direction, but it is best for one direction.

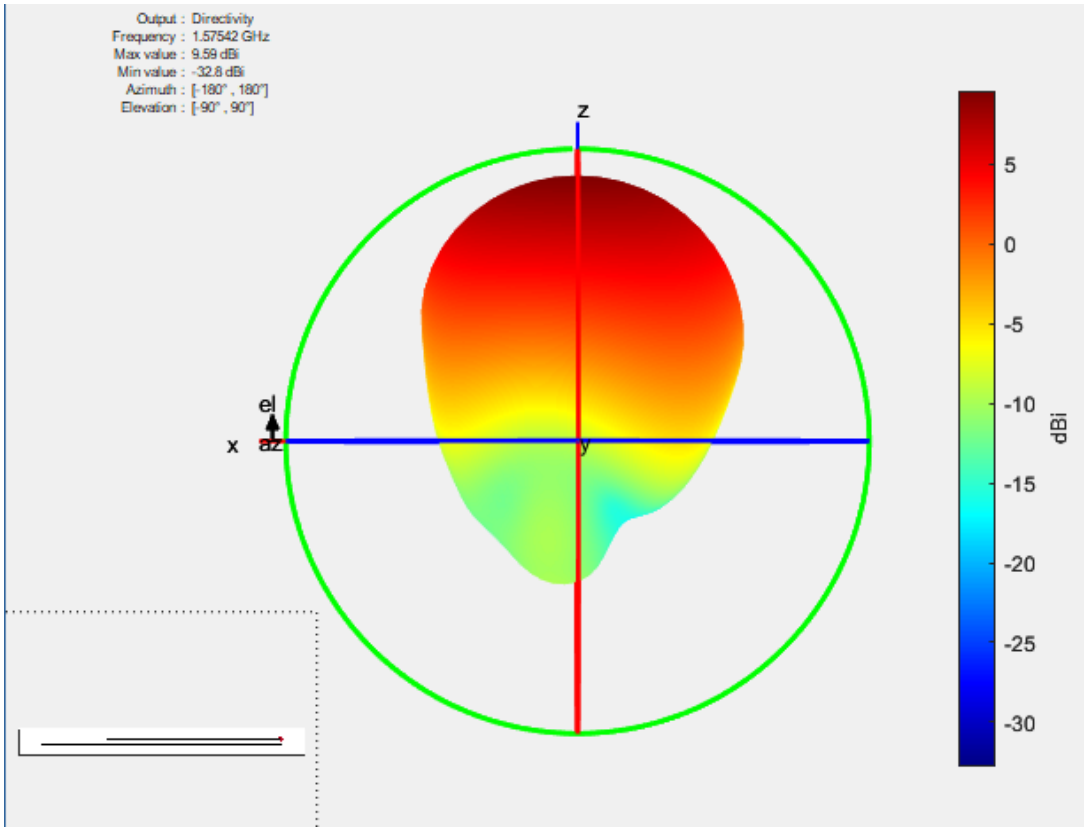

Figure 44 : Gain for Main Patch Antenna

Here, in the figure above, you can see the gain "lobes" for the main antenna. Where in the positive Z-direction is a longer lobe and therefore a stronger signal gain. Therefore, in the left bottom corner where we see a diagram of the orientation of the antenna, we know how the antenna should be mounted in respect to the CubeSat.

Planar Inverted-F (PIF) Antenna

The PIF Antenna is a different type of patch antenna and is much less common than the typical infed patch antenna. Again, it is a directional patch antenna but the plane that is directional is perpendicular to the previous axis. And additionally, to reiterate why there is a secondary antenna is to help ensure continuous coverage of the GPS constellation and to ensure that the mission critical data is good.

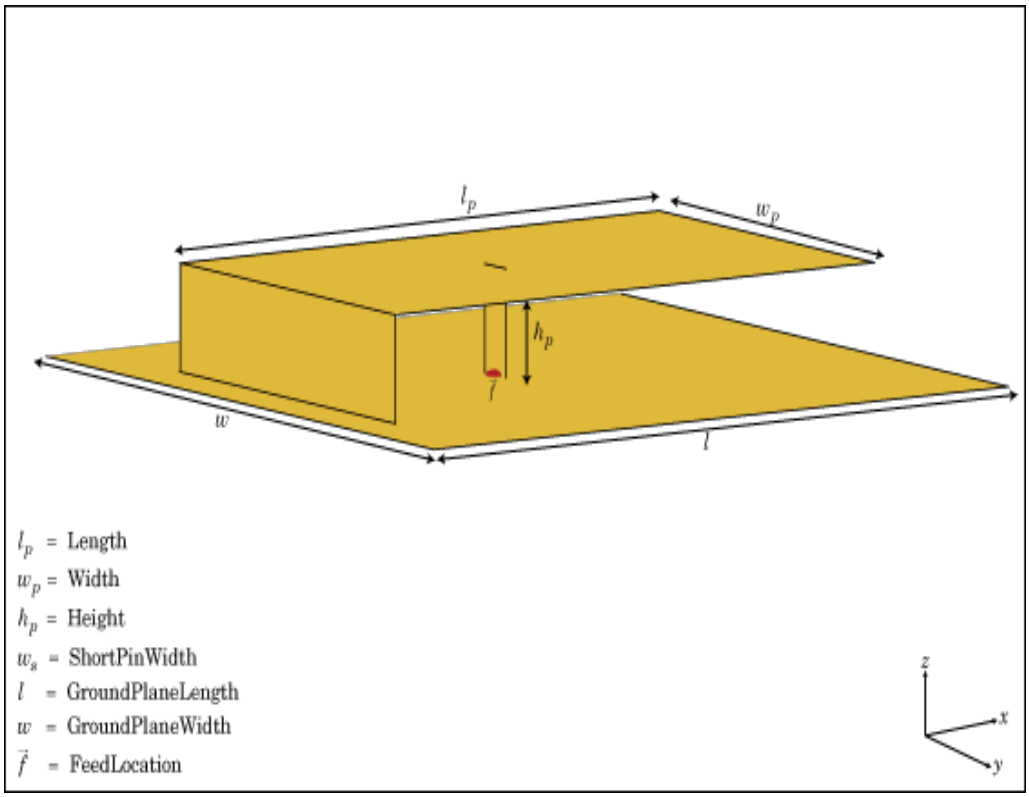

Figure 45 : Diagram of PIF Antenna [From MATLAB Antenna Designer App]

Above is a general layout of a PIF Antenna using the MATLAB antenna designer application. The general design of the patch antenna is like that of a normal patch other than the ground element being connected to the radiating element, this in turn changes the characteristics of the transmitting and receiving capabilities of the antenna.

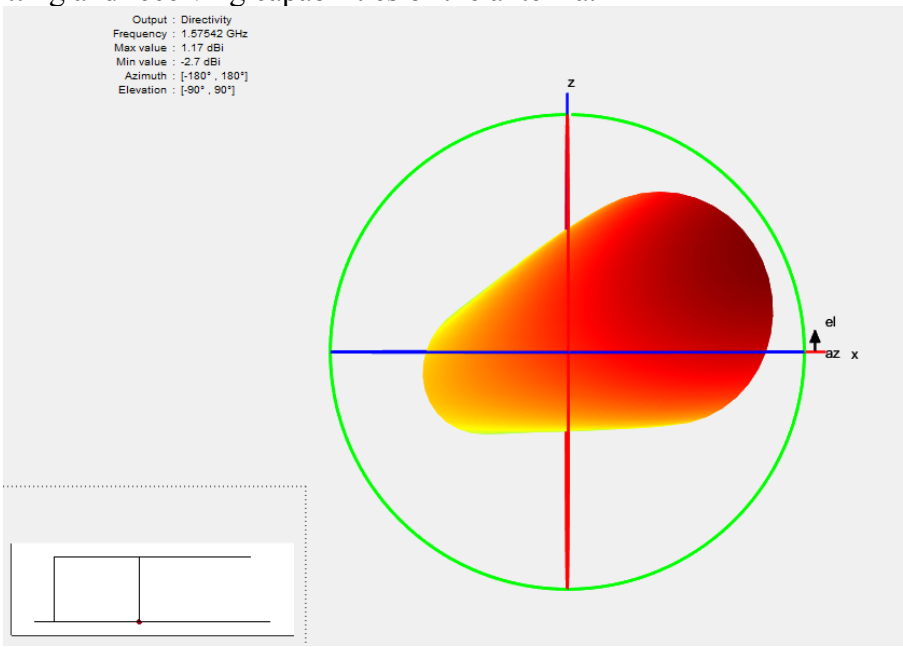

Figure 46 : 3D Gain plot of PIF Antenna

Above is a gain plot for the PIF antenna design in which you see that the gain is stronger 90 degrees to the regular patch antenna. This is useful as this antenna is designed to be at the top of the nadir-out direction solar panels to ensure a good strong signal by being the only item with a complete “view” of the GPS network.

Appendix D

Alternative UHF Unit

While the COTS unit for UHF is not a bad radio, it is rather low power and expensive for its capabilities and so we are providing an alternative option which would also work in this application. Now is the time to talk more about the actual radio itself as it is based on the Analog Devices ADF7023-J which is the basis of the homegrown UHF communications system.

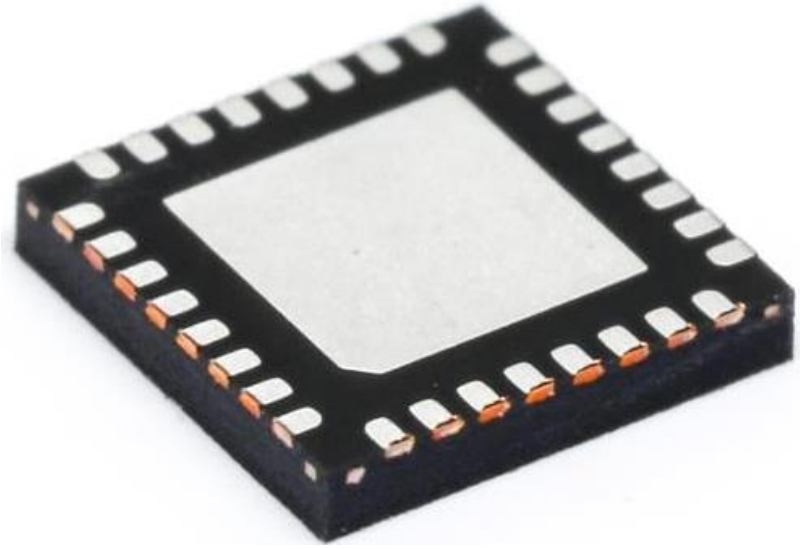

Figure 47 : Analog Devices ADF7023-J (Courtesy of Mouser Electronics) [57].

This chipset is very power efficient and is extremely small and rather easy to implement as it is very well documented. It can be the center of a 5-watt RF power transceiver system, which would easily have the bandwidth and power for a backup communications system.

This unit is a single part of the radio, but it is the muscle of the system while the microcontroller is the brains of the radio. This chipset would work rather well as it is particular well suited for the environment of space and the mission. However, this was not explored much farther due to time constraints and difficulty with verification that this backup radio system would be space ready. As a result, it is important to note but was no included in the final design as to help increase the technology readiness level of the entire CubeSat.

Appendix E

Testbed CubeSat Control Board PCB design [72].

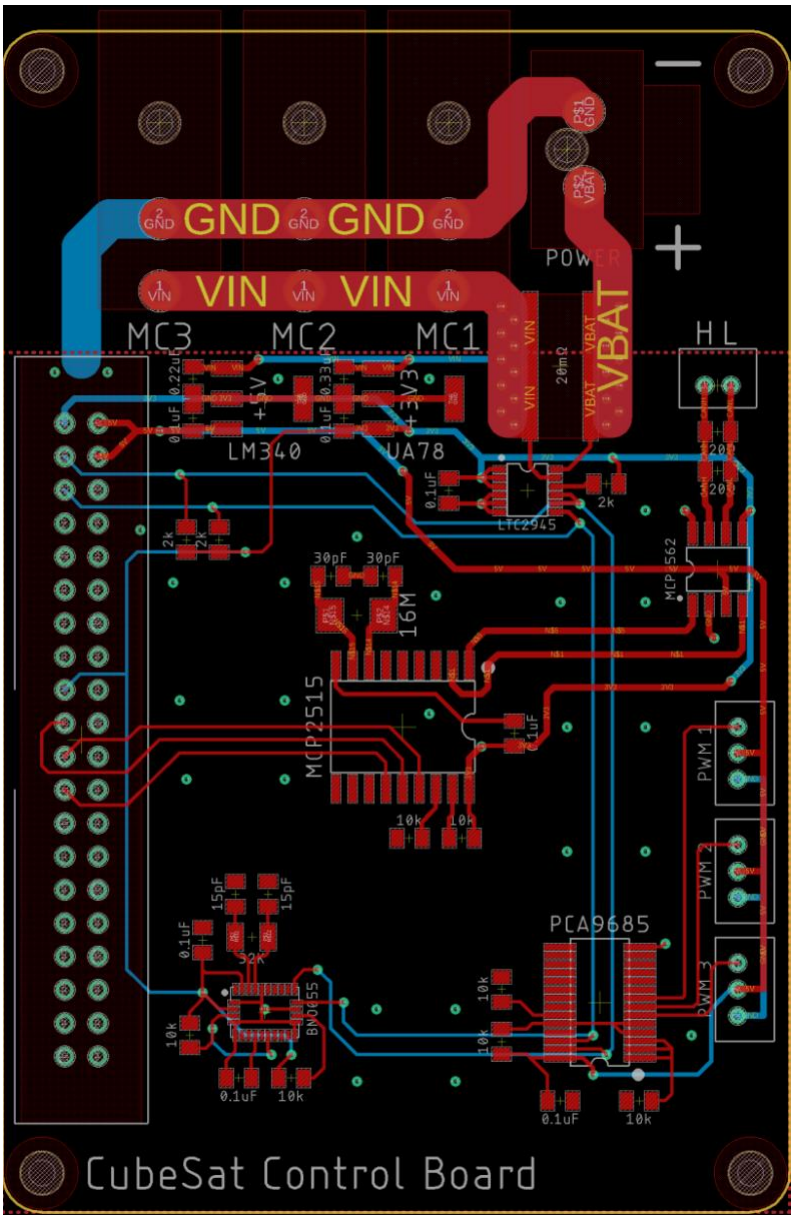

Appendix F

CubeSat Control Board test stand schematic [72].